Available online at www.sciencedirect.com
ScienceDirect
Comput. Methods Appl. Mech. Engrg. 197 (2008) 2930–2947
Computer methods in applied mechanics and engineering
www.elsevier.com/locate/cma

A discontinuous Galerkin finite element model for river bed evolution under shallow flows

P.A. Tassi [a,b], S. Rhebergen [a], C.A. Vionnet [b], O. Bokhove [a,*]

[a] Department of Applied Mathematics, Institute of Mechanics, Processes and Control, Twente, University of Twente, P.O. Box 217, 7500 AE, Enschede, The Netherlands
[b] Department of Engineering and Water Resources, Universidad Nacional del Litoral & Conicet Santa Fe, Argentina

Received 29 May 2007; received in revised form 6 November 2007; accepted 24 January 2008
Available online 15 February 2008

Abstract

The accurate representation of morphodynamic processes and the ability to propagate changes in the riverbed over a wide range of space and time scales make the design and implementation of appropriate numerical schemes challenging. In particular, requirements of accuracy and stability for medium and long term simulations are difficult to meet. In this work, the derivation, design, and implementation of a discontinuous Galerkin finite element method (DGFEM) for sediment transport and bed evolution equations are presented. Numerical morphodynamic models involve a coupling between a hydrodynamic flow solver which acts as a driving force and a bed evolution model which accounts for sediment flux and bathymetry changes. A space DGFEM is presented based on an extended approach for systems of partial differential equations with non-conservative products, in combination with two intertwined Runge–Kutta time stepping schemes for the fast hydrodynamic and slow morphodynamic components. The resulting numerical scheme is verified by comparing simulations against (semi-)analytical solutions. These include the evolution of an initially symmetric, isolated bedform; the formation and propagation of a step in a straight channel due to a sudden overload of sediment discharge; the propagation of a travelling diffusive sediment wave in a straight channel; and, the evolution of an initially flat bed in a channel with a contraction. Finally, a comparison is made between a numerical simulation and field data of a trench excavated in the main channel of the Paraná river near Paraná city, Argentina.

Keywords: Discontinuous Galerkin finite element method; Morphodynamic model; Shallow flows; Non-conservative products; Multiphase physics

1. Introduction

Quantifying the interaction between sediment transport and water flow plays an important role in many river and coastal engineering applications. Traditionally, research on river processes was primarily based on field observations and laboratory scale modelling. Laboratory scale models have been essential for understanding complex river processes and as design and verification tools, despite their high cost of construction, maintenance and operation. Field measurements are also costly and difficult to realize especially for large-scale systems. An alternative that has been growing in popularity and acceptance is mathematical and numerical modelling of river flows. River modelling is the simulation of flow conditions based on the formulation and solution of a mathematical model or a discretization thereof expressing conservation laws. Predictions of morphodynamic changes of the bed in natural channels integrate different physical mechanisms acting within the system according to their time response, i.e., we are dealing with a multi-scale problem. These relevant mechanisms that drive morphodynamic changes of alluvial rivers are: (i) hydrodynamics, with conservation laws of mass and momentum; (ii) bed evolution, with a conservation law for sediment mass; and, (iii) sediment transport, with predictors for the sediment carrying capacity of the river.

* Corresponding author. Tel.: +31 (0)53 4893412; fax: +31 (0)53 4894833.
E-mail address: o.bokhove@math.utwente.nl (O. Bokhove).

0045-7825/$ - see front matter © 2008 Elsevier B.V. All rights reserved.
doi:10.1016/j.cma.2008.01.023

The entire system is often referred to as a *morphodynamic model*.

There are particular difficulties associated with solving hyperbolic partial differential equations, including the propagation of sediment bores or discontinuous steps in the bedform, which must be overcome by a good numerical scheme. There exist many different numerical methods to solve the system of conservation laws of water and sediment. We have chosen the discontinuous Galerkin finite element method (DGFEM) for the numerical solution of the morphodynamic model. Among other advantages, the accuracy and local nature of the numerical scheme make it suitable for these morphodynamic problems. Furthermore, conservation of the transported quantity is satisfied on a local or elemental level. For a DGFEM discretization of hydrodynamic shallow water flows, we refer to [1]. Here we extend and refine that method to include the bed evolution as well. A partly non-conservative formulation is used that allows the application of the unified space and space–time discontinuous Galerkin discretization for hyperbolic systems of partial differential equations with non-conservative products developed in [2] to solve the entire morphodynamic model. In our case, the non-conservative product consists of the topographic terms present in the momentum equations. For the diffusive term in the bed evolution equation, we used the primal formulation of [3–5]. Additionally, we made use of advanced time stepping schemes to deal with the multi-scale property of the morphodynamic problem. In summary, novel in this work are: (I) the application of the discontinuous Galerkin finite element discretization to systems with non-conservative products developed in [2] to solve the hydrodynamic and bed evolution model; (II) the implementation of the primal formulation to deal with the downhill rolling sediment term present in the sediment transport formula; (III) the verification of the results of the DGFEM with a survey of original (semi-)analytical solutions; and, (IV) the validation of these computed results against measurements.

The outline of the paper is as follows. The governing equations and the scaling are introduced in Section 2. The spatial discretization of the DGFEM is introduced in Section 3. A time discretization is required to solve the ordinary differential equations that emerge from the spatial finite element discretization. Numerical complications arise due to the presence of a small parameter ϵ in front of the time derivatives in the depth and momentum equations. Here, ϵ expresses the ratio of the fast hydrodynamic time scale and the slow sediment transport time scale. However, a set of differential–algebraic equations emerges in the limit $\epsilon \to 0$. The essentials of the time stepping procedure for space DGFEM are described in Section 3.6. In Section 4, the numerical scheme is verified by comparing simulations with (semi-)analytical solutions. A comparison between the numerical model and field data of a trench excavated in the main channel of the Paraná river (Argentina) is used as validation test in Section 5. At several instances, we also mention the intercomparison of the space DGFEM presented here with the space–time DGFEM developed in [2], and extended here to our morphodynamical application. Conclusions are drawn in Section 6.

2. Governing equations and scaling

A system of hydrodynamic and bed evolution equations is introduced. Both the hydrodynamic and morphodynamic components of this system are based on a depth-average over the water column. We present these hydrodynamic and morphodynamic components first in separation before combining them.

2.1. Hydrodynamic shallow water equations

The shallow water equations (SWE) in nearly conservative form read (cf. [6])

$$\begin{aligned}&\partial_{t^*} h^* + \nabla^* \cdot (h^* \mathbf{u}^*) = 0,\\ &\partial_{t^*}(h^* \mathbf{u}^*) + \nabla^* \cdot (h^* \mathbf{u}^* \mathbf{u}^*) + g \nabla^* (h^{*2}/2)\\ &\quad = -g h^* \nabla^* b^* - \boldsymbol{\tau}_{\mathrm{b}}^*/\rho^*,\end{aligned} \tag{2.1}$$

where partial derivatives are denoted by $\partial_{t^*} = \partial/\partial t^*$ and so forth; $\nabla^* = (\partial_{x^*}, \partial_{y^*})^{\mathrm{T}}$ with transpose $(\cdot)^{\mathrm{T}}$; $\mathbf{u}^*(\mathbf{x}^*, t^*) = (u^*(\mathbf{x}^*, t^*), v^*(\mathbf{x}^*, t^*))^{\mathrm{T}}$ is the depth-averaged velocity as function of horizontal coordinates $\mathbf{x}^* = (x^*, y^*)^{\mathrm{T}}$ and time t^*; and the free surface resides at $z^* = h^* + b^*$ with $h^*(\mathbf{x}^*, t^*)$ the total water depth and $b^*(\mathbf{x}^*, t^*)$ the elevation of the bottom topography above datum, both measured along the vertical coordinate z^*, and aligned against the direction of the acceleration of gravity of magnitude g. A relationship for the bed resistance term $\boldsymbol{\tau}_{\mathrm{b}}^* = (\tau_{\mathrm{bx}}^*, \tau_{\mathrm{by}}^*)^{\mathrm{T}}$ must be specified and the classical quadratic dependency on the depth-averaged velocity is adopted:

$$\boldsymbol{\tau}_{\mathrm{b}}^* = \rho^* C_{\mathrm{f}}^* |\mathbf{u}^*| (u^*, v^*)^{\mathrm{T}} \quad \text{with } |\mathbf{u}^*| = \sqrt{u^{*2} + v^{*2}}, \tag{2.2}$$

a constant friction coefficient C_{f}^*, and constant density ρ^*.

2.2. Sediment continuity equation

The evolution of the bed $b^*(\mathbf{x}^*, t^*)$ is governed by a sediment continuity equation [7–10]

$$\partial_{t^*} b^* + \nabla^* \cdot \mathbf{q}_{\mathrm{b}}^* = 0 \tag{2.3}$$

with volumetric bed load sediment flux $\mathbf{q}_{\mathrm{b}}^*(\mathbf{x}^*, t^*) = (q_{\mathrm{bx}}^*, q_{\mathrm{by}}^*)^{\mathrm{T}}$ through a vertical cross section of the bed. We adopt a simple power-law form of transport for noncohesive sediment of uniform grain size [7], and include the downslope gravitational transport component that generalizes ideas going back to the earlier work of [11]. Thus, we close (2.3) with

$$\mathbf{q}_{\mathrm{b}}^* = \alpha^* |\mathbf{u}^*|^{\beta} (\mathbf{u}^*/|\mathbf{u}^*| - \kappa^* \nabla^* b^*), \tag{2.4}$$

where α^* is a proportionality factor including the bed material porosity, β a constant, and the diffusive term with $\kappa^* \nabla^* b^*$ is a bed slope correction term accounting for the preferred downslope transport of sediment with nondimensional proportionality constant κ^*. For various slowly

varying alluvial flows, it has been deduced that $1 < \beta \leqslant 3$. However, larger values of β may be attained when the bed is covered by dunes. Most empirical bed load sediment transport functions available are given in forms akin to (2.4) with $\mathbf{q}_{\mathrm{b}}^*$ depending monotonically on the flow speed, and α^* constant [12].

Finally, the system (2.1),(2.2),(2.3) and (2.4) is considered in a bounded domain $\Omega \subset \mathbb{R}^2$. It is completed with initial conditions $h^*(\mathbf{x}^*,0), \mathbf{u}^*(\mathbf{x}^*,0)$, and $b^*(\mathbf{x},0)$, and boundary conditions such as in- and outflow, and/or slip flow along solid walls. The sediment transport equation emerges as a mixed hyperbolic and parabolic equation, and extra boundary conditions are required involving b^* and the sediment flux. Relevant boundary conditions will be discussed later in the applications.

2.3. Scaling

It is convenient to treat the governing equations in nondimensional form for computational reasons and to clarify the coupling of the hydrodynamics to the dynamics of the bed. Sediment transport of the bed occurs on a transport time scale much longer than the flow time scale (cf. [13]). It is, of course, possible to scale the dimensionless results back to dimensional results a posteriori, and for a range of scalings with the same dimensionless numbers.

First, we consider a simple solution to systems (2.1) and (2.3). Uniform one-dimensional flow down an inclined plane along x^* with constant slope S_0 satisfies

$$\begin{aligned}
&\mathbf{u}^*(\mathbf{x}^*,t^*) = (u_0^*,0)^{\mathrm{T}}, \quad \boldsymbol{\tau}_{\mathrm{b}}^* = (\tau_{\mathrm{b}0}^*,0)^{\mathrm{T}}, \quad \mathbf{q}_{\mathrm{b}}^*(\mathbf{x}^*,t^*) = (q_{\mathrm{b}0}^*,0)^{\mathrm{T}},\\
&h^*(\mathbf{x}^*,t^*) = h_0^*, \quad u_0^* = \sqrt{g h_0^* S_0 / C_{\mathrm{f}}^*}, \quad q_0^* = h_0^* u_0^*,\\
&q_{\mathrm{b}0}^* \approx \alpha^* u_0^{*\beta}, \quad \tau_{\mathrm{b}0}^* = \rho^* C_{\mathrm{f}}^* u_0^{*2},
\end{aligned} \tag{2.5}$$

given the water discharge q_0^*, sediment flux $q_{\mathrm{b}0}^*$, and constant friction coefficient C_{f}^*. This solution suggests the use of the following scaling:

$$\begin{aligned}
&\mathbf{x} = \mathbf{x}^*/l_0^*, \quad t = t^*/t_0^*, \quad h = h^*/h_0^*, \quad b = b^*/h_0^*,\\
&\mathbf{u} = \mathbf{u}^*/u_0^*, \quad \mathbf{q}_{\mathrm{b}} = \mathbf{q}_{\mathrm{b}}^*/(\alpha^* u_0^{*\beta}), \quad \text{and} \quad t_0^* = h_0^* l_0^*/q_{\mathrm{b}0}^*,
\end{aligned} \tag{2.6}$$

where l_0^*, t_0^*, h_0^* and u_0^* are characteristic length, time, depth and velocity scales, respectively. We have chosen t_0^* to be the sediment transport time scale associated with the erosion and deposition of sediment.

Substitution of the above scaling (2.6) into system (2.1)–(2.3) and (2.4) yields the nondimensional system

$$\epsilon \partial_t h + \nabla\cdot(h\mathbf{u}) = 0, \tag{2.7a}$$

$$\epsilon \partial_t (h\mathbf{u}) + \nabla\cdot(h\mathbf{u}\mathbf{u}) + \mathsf{F}^{-2}\nabla(h^2/2) = -\mathsf{F}^{-2} h\nabla b - C_{\mathrm{f}}\mathbf{u}|\mathbf{u}|, \tag{2.7b}$$

$$\partial_t b + \nabla\cdot\mathbf{q}_{\mathrm{b}} = 0, \tag{2.7c}$$

with the nondimensional sediment flux

$$\mathbf{q}_{\mathrm{b}} = |\mathbf{u}|^{\beta}(\mathbf{u}/|\mathbf{u}| - \kappa\nabla b), \tag{2.7d}$$

where $\mathbf{q}_{\mathrm{b}} = (q_{\mathrm{b}x}, q_{\mathrm{b}y})^{\mathrm{T}}$ and $\nabla = (\partial_x, \partial_y)^{\mathrm{T}}$. In this system, the following parameters have emerged: the nondimensional friction coefficient $C_{\mathrm{f}} = \gamma C_{\mathrm{f}}^* = (l_0^*/h_0^*)C_{\mathrm{f}}^*$, the ratio between the flow velocity and surface gravity-wave speed or Froude number $\mathsf{F} = u_0^*/\sqrt{g h_0^*}$, a scaled $\kappa = \kappa^* h_0^*/l_0^*$, and the ratio between sediment and hydrodynamic discharge $\epsilon = \alpha^* u_0^{*\beta}/u_0^* h_0^* = q_{\mathrm{b}0}^*/q_0^*$.

Most rivers transport far less sediment than water, so the condition $\epsilon \ll 1$ prevails even during floods. The parameter ϵ typically attains values in the range 10^{-3}–10^{-6} [14], which at leading order in ϵ makes the hydrodynamic equations stationary and algebraic. For $\epsilon \ll 1$ the hydrodynamic equations are therefore nearly *quasi-stationary* on the sediment time scale.

3. Space discontinuous Galerkin discretization

3.1. Concise formulation

To facilitate the discretization, the scaled system (2.7a)–(2.7d) is written concisely as follows:

$$A_{ir}\partial_t U_r + F_{ik,k} + G_{ikr}U_{r,k} - (T_i\delta_{ij}U_{j,k})_{,k} = S_i \tag{3.1}$$

for $i,j,r = 1,2,3,4$ and $k = 1,2$ with

$$U = \begin{bmatrix} h \\ hu \\ hv \\ b \end{bmatrix}, \quad A = \begin{bmatrix} \epsilon & 0 & 0 & 0 \\ 0 & \epsilon & 0 & 0 \\ 0 & 0 & \epsilon & 0 \\ 0 & 0 & 0 & 1 \end{bmatrix}, \tag{3.2}$$

$$F(U) = \begin{bmatrix} hu & hv \\ hu^2 + \mathsf{F}^{-2}h^2/2 & huv \\ huv & hv^2 + \mathsf{F}^{-2}h^2/2 \\ |\mathbf{u}|^{\beta-1}u & |\mathbf{u}|^{\beta-1}v \end{bmatrix}, \tag{3.3}$$

$$G_1(U) = \begin{bmatrix} 0 & 0 & 0 & 0 \\ 0 & 0 & 0 & \mathsf{F}^{-2}h \\ 0 & 0 & 0 & 0 \\ 0 & 0 & 0 & 0 \end{bmatrix}, \quad G_2(U) = \begin{bmatrix} 0 & 0 & 0 & 0 \\ 0 & 0 & 0 & 0 \\ 0 & 0 & 0 & \mathsf{F}^{-2}h \\ 0 & 0 & 0 & 0 \end{bmatrix}, \tag{3.4}$$

$T_1 = T_2 = T_3 = 0$, and $T = T_4 = \kappa|\mathbf{u}|^{\beta}$, and

$$S(U) = \begin{bmatrix} 0 \\ -C_{\mathrm{f}}|\mathbf{u}|u \\ -C_{\mathrm{f}}|\mathbf{u}|v \\ 0 \end{bmatrix}. \tag{3.5}$$

Derivatives in space are denoted by the comma subscript notation $(\cdot)_{,k} = \partial_{x_k}(\cdot)$ with $k = 1,2$ and $\mathbf{x} = (x_1,x_2)^{\mathrm{T}}$. The only non-conservative terms in (3.1) are the topographic terms in the momentum equations.

The weak formulation starts with a first-order reformulation of system (3.1), as follows:

$$A_{ir}\partial_t U_r + F_{ik,k} + G_{ikr}U_{r,k} - \delta_{i4}\Theta_{k,k} = S_i \quad \text{for } i,r = 1,2,3,4, \tag{3.6a}$$

$$\Theta_k = TU_{4,k} \quad \text{and} \quad k = 1,2. \tag{3.6b}$$

3.2. Space elements, function space and operators

The flow domain $\Omega \subset \mathbb{R}^2$ is a bounded area which in turn is partitioned into N_{el} elements K_{k}. It consists of segments $\partial\Omega_{\mathrm{s}}$ demarcating a fixed boundary and open boundary segments $\partial\Omega_{\mathrm{o}}$ such that $\partial\Omega = \partial\Omega_{\mathrm{s}} \cup \partial\Omega_{\mathrm{o}}$. The tessellation of the domain Ω is

$$\mathscr{T}_h = \left\{ K_{\mathsf{k}} \Big| \bigcup_{\mathsf{k}=1}^{N_{\mathrm{el}}} \overline{K}_{\mathsf{k}} = \overline{\Omega}_{\mathsf{h}} \text{ and } K_{\mathsf{k}} \cap K_{\mathsf{k}'} = 0 \text{ if } \mathsf{k} \neq \mathsf{k}', 1 \leqslant \mathsf{k}, \mathsf{k}' \leqslant N_{\mathrm{el}} \right\}, \tag{3.7}$$

such that $\Omega_{\mathsf{h}} \to \Omega$ as $\mathsf{h} \to 0$ with h the smallest radius of all circles completely containing the elements $K_{\mathsf{k}} \in \mathscr{T}_h$. Here $\overline{K}_{\mathsf{k}}$ is the closure of K_{k} (and likewise for $\overline{\Omega}$). A reference element $\widehat{K}$ is introduced with the mapping

$$F_{K_{\mathsf{k}}} : \widehat{K} \mapsto K_{\mathsf{k}} : \bar{\xi} \mapsto \mathbf{x} := \sum_j \mathbf{x}_j \chi_j(\bar{\xi}), \tag{3.8}$$

where $\bar{\xi} = (\xi_1, \xi_2)$ are the reference coordinates, $\mathbf{x}_j$ are the coordinates of the local nodes of the element, with $j = 1, \ldots, N_{\mathsf{k}}$, $\chi_j(\bar{\xi})$ the standard shape functions used in finite elements, and N_{k} the number of nodes in element k. For quadrilateral elements $N_{\mathsf{k}} = 4$ and for triangular elements $N_{\mathsf{k}} = 3$. In general, the element boundary ∂K_{k} is connected through faces $\mathscr{S}$ either to its neighboring elements or to the boundary of the domain.

In each reference element $\widehat{K}$ a set of polynomials of order p is defined, represented by $P_k(\widehat{K})$ with $k = 0, \ldots, n_p - 1$ for positive integers p and n_p. For the discontinuous Galerkin discretization of (3.6a) we define the space V_h of discontinuous test functions

$$V_h = \{ V \in (L^2(\Omega_h))^4 | \forall K_{\mathsf{k}} \in \mathscr{T}_h : V|_{K_{\mathsf{k}}} \circ F_K \in (\mathscr{P}_{p_k}(K_{\mathsf{k}}))^4 \} \tag{3.9}$$

with $\mathscr{P}_{pk}(K_{\mathsf{k}})$ the usual space of polynomials on K_{k} of degree equal to or less than $p_k \leqslant p$ and $L^2(\Omega_h)$ the space of square integrable functions on Ω_h. For the discontinuous Galerkin discretization of (3.6b) we define the space W_h of discontinuous test vector functions

$$W_h = \{ W \in (L^2(\Omega_h))^{n_{\mathrm{s}} \times d} | \forall K_{\mathsf{k}} \in \mathscr{T}_h : W|_{K_{\mathsf{k}}} \circ F_{K_{\mathsf{k}}} \in (\mathscr{P}_{p_k}(K_{\mathsf{k}}))^{n_{\mathrm{s}} \times d} \} \tag{3.10}$$

for dimension $d = 2$. These definitions are such that for system size $n_{\mathrm{s}} = 4$ we have $\nabla V_h \subset W_h$.

For a function $V \in V_h$ and function $W \in W_h$ the traces on an element boundary ∂K are defined as

$$V^{\mathsf{L}} = \lim_{\varepsilon \downarrow 0} V(\mathbf{x} - \varepsilon n^{\mathsf{L}}) \quad \text{and} \quad W^{\mathsf{L}} = \lim_{\varepsilon \downarrow 0} W(\mathbf{x} - \varepsilon n^{\mathsf{L}}) \tag{3.11}$$

with n^{L} the unit outward normal vector of the boundary ∂K, also K_{L} and K_{R} are the elements left or right of a face $\mathscr{S}$. Faces $\mathscr{S}$ of elements are either internal faces $\mathscr{S}_{\mathrm{I}}$ or boundary faces $\mathscr{S}_{\mathrm{B}}$. The averages or means of a function $V \in V_h$ on an internal and boundary face are

$$\{\!\{V\}\!\} = (V^{\mathsf{L}} + V^{\mathsf{R}})/2 \text{ on } \mathscr{S}_{\mathrm{I}}, \quad \{\!\{V\}\!\} = V^{\mathsf{L}} \text{ on } \mathscr{S}_{\mathrm{B}}, \tag{3.12}$$

such that at a boundary face we always take the interior or left value. Likewise, for a function $W \in W_h$ the mean values are

$$\{\!\{W\}\!\} = (W^{\mathsf{L}} + W^{\mathsf{R}})/2 \text{ on } \mathscr{S}_{\mathrm{I}}, \quad \{\!\{W\}\!\} = W^{\mathsf{L}} \text{ on } \mathscr{S}_{\mathrm{B}}. \tag{3.13}$$

The jumps of a function $V \in V_h$ on an internal and boundary face are

$$[\![V]\!]_k = V^{\mathsf{L}} n_k^{\mathsf{L}} + V^{\mathsf{R}} n_k^{\mathsf{R}} \text{ on } \mathscr{S}_{\mathrm{I}}, \quad [\![V]\!]_k = V^{\mathsf{L}} n_k^{\mathsf{L}} \quad \text{on } \mathscr{S}_{\mathrm{B}} \tag{3.14}$$

such that at a boundary face we always take the interior left value, and where n^{L} and n^{R} are the outward normal vectors of elements K_{L} and K_{R} with $n^{\mathsf{R}} = -n^{\mathsf{L}}$. Likewise, for a function $W \in W_h$ the jumps are

$$[\![W]\!]_k = W_k^{\mathsf{L}} n_k^{\mathsf{L}} + W_k^{\mathsf{R}} n_k^{\mathsf{R}} \text{ on } \mathscr{S}_{\mathrm{I}}, \quad [\![W]\!]_k = W_k^{\mathsf{L}} n_k^{\mathsf{L}} \text{ on } \mathscr{S}_{\mathrm{B}}. \tag{3.15}$$

A useful property for $V \in V_h$ and $W \in W_h$ on internal faces is

$$[\![V_i W_k]\!]_k = \{\!\{V_i\}\!\} [\![W_k]\!]_k + [\![V_i]\!]_k \{\!\{W_k\}\!\}. \tag{3.16}$$

Hereafter, we will often combine the sum over internal and boundary faces by defining a suitable ghost value U^{R} at the boundary faces.

In the next section, we will also use the following relation for the element boundary integrals which occur in the weak formulation

$$\sum_{K_{\mathsf{k}}} \int_{\mathscr{S}} V_i^{\mathsf{L}} W_k^{\mathsf{L}} n_k^{\mathsf{L}} \mathrm{d}\mathscr{S} = \sum_{\mathscr{S} \in \mathscr{S}_{\mathrm{I}}} \int_{\mathscr{S}} [\![V_i W_k]\!]_k \mathrm{d}\mathscr{S} + \sum_{\mathscr{S} \in \mathscr{S}_{\mathrm{B}}} \int_{\mathscr{S}} V_i^{\mathsf{L}} W_k^{\mathsf{L}} n_k^{\mathsf{L}} \mathrm{d}\mathscr{S}. \tag{3.17}$$

On internal faces, the following relations hold:

$$\{\!\{\{\!\{F\}\!\}\}\!\} = \{\!\{F\}\!\} \quad \text{and} \quad [\![\{\!\{F\}\!\}]\!]_k = 0. \tag{3.18}$$

3.3. Weak formulation

A flux formulation is obtained after multiplying (3.6a) by an arbitrary test function $V \in V_h$, using the non-conservative weak formulation in [2] (their expression (A.11)) for the hyperbolic terms, integrating the diffusive term by parts, and summing over all elements

$$\sum_{K_k}\int_{K_k}(V_iA_{ir}\partial_t U_r - V_{i,k}F_{ik} + V_iG_{ikr}U_{r,k} + V_{i,k}\delta_{i4}\Theta_k - V_iS_i) \times \mathrm{d}K + \sum_{\mathscr{S}}\int_{\mathscr{S}}\left((V_i^{\mathsf{L}} - V_i^{\mathsf{R}})(\{\!\{F_{ik}\}\!\}n_k^{\mathsf{L}} + \widetilde{H}_i^{\mathrm{nc}}) + \{\!\{V_i\}\!\}\int_0^1 G_{ikr}(\phi(\tau;U^{\mathsf{L}},U^{\mathsf{R}}))\frac{\partial\phi_r}{\partial\tau}(\tau;U^{\mathsf{L}},U^{\mathsf{R}})\mathrm{d}\tau n_k^{\mathsf{L}}\right)\mathrm{d}\mathscr{S} - \sum_{K_k}\int_{\partial K}V_i^{\mathsf{L}}\delta_{i4}\Theta_k^{\mathsf{L}}n_k^{\mathsf{L}}\mathrm{d}\mathscr{S} = 0 \tag{3.19}$$

with $\mathrm{d}K$ an elemental area and $\mathrm{d}\mathscr{S}$ a line element on a face $\mathscr{S}$, $\widetilde{H}_i^{\mathrm{nc}}$ a stabilizing flux term in the non-conservative treatment, defined later. A linear path $\phi(\tau;U^{\mathsf{L}},U^{\mathsf{R}}) = U^{\mathsf{L}} + \tau(U^{\mathsf{R}} - U^{\mathsf{L}})$ connecting the left and right states across the discontinuity is adopted. The integrals containing the linear path are either evaluated analytically or with two-point Gauss quadrature. For details on the non-conservative discontinuous Galerkin formulation for the hyperbolic part, we refer to [2].

3.4. The auxiliary variable

Our aim is to eliminate in (3.19) the auxiliary variable Θ_k for the interior elements. Storage space is thus saved. Multiplication of (3.6b) by arbitrary test functions $W \in W_h$, integration by parts back and forth, and summation over the elements yields

$$\sum_{K_k}\int_{K_k}W_k(\Theta_k - TU_{4,k})\mathrm{d}K - \sum_{K_k}\int_{\partial K}W_k^{\mathsf{L}}T^{\mathsf{L}}(\widehat{U}_4 - U_4^{\mathsf{L}})n_k^{\mathsf{L}}\mathrm{d}\mathscr{S} = 0, \tag{3.20}$$

where we introduced a numerical flux $\widehat{U}_4$ only in the forward integration by parts. The boundary term in (3.20) is analyzed again by changing the elemental summation to a face summation, and the use of relations (3.16) and (3.18), to obtain

$$\sum_{K_k}\int_{\partial K}W_k^{\mathsf{L}}T^{\mathsf{L}}(\widehat{U}_4 - U_4^{\mathsf{L}})n_k^{\mathsf{L}}\mathrm{d}\mathscr{S} = \sum_{\mathscr{S}\in\mathscr{S}_{\mathrm{I}}}\int_{\mathscr{S}}[\![W_kT(\widehat{U}_4 - U_4)]\!]_k\mathrm{d}\mathscr{S} + \sum_{\mathscr{S}\in\mathscr{S}_{\mathrm{B}}}\int_{\mathscr{S}}W_k^{\mathsf{L}}T^{\mathsf{L}}(\widehat{U}_4 - U_4^{\mathsf{L}})n_k^{\mathsf{L}}\mathrm{d}\mathscr{S}. \tag{3.21}$$

We now introduce the numerical flux

$$\widehat{U}_4 = \begin{cases}\{\!\{U_4\}\!\} & \text{at } \mathscr{S}_{\mathrm{I}},\\ U_4^B & \text{at } \mathscr{S}_{\mathrm{B}}.\end{cases} \tag{3.22}$$

With this choice for the numerical flux at the internal faces and by using relations (3.17) and (3.18), we obtain: $[W_kT(\widehat{U}_4 - U_4)]_k = -\{\!\{W_kT\}\!\}[\![U_4]\!]_k$. Hence, (3.20) becomes

$$\sum_{K_k}\int_{K_k}W_k(\Theta_k - TU_{4,k})\mathrm{d}K = -\sum_{\mathscr{S}\in\mathscr{S}_{\mathrm{I}}}\int_{\mathscr{S}}\{\!\{W_kT\}\!\}[\![U_4]\!]_k\mathrm{d}\mathscr{S} - \sum_{\mathscr{S}\in\mathscr{S}_{\mathrm{B}}}\int_{\mathscr{S}}W_k^{\mathsf{L}}T^{\mathsf{L}}(U_4^{\mathsf{L}} - U_4^B)n_k^{\mathsf{L}}\mathrm{d}\mathscr{S}. \tag{3.23}$$

To obtain an explicit expression for the auxiliary variable, we define a *global lifting operator* $\mathscr{R} \in W_h$, which is defined in the weak sense as: find an $\mathscr{R} \in W_h$ such that for all $W \in W_h$

$$\sum_{K_k}\int_{K_k}W_k\mathscr{R}_k\mathrm{d}K = \sum_{S\in\mathscr{S}_{\mathrm{I}}}\int_{\mathscr{S}}\{\!\{TW_k\}\!\}[\![U_4]\!]_k\mathrm{d}\mathscr{S} + \sum_{S\in\mathscr{S}_{\mathrm{B}}}\int_{\mathscr{S}}W_k^{\mathsf{L}}T^{\mathsf{L}}(U_4^{\mathsf{L}} - U_4^B)n_k^{\mathsf{L}}\mathrm{d}\mathscr{S}. \tag{3.24}$$

Details on the solvability of (3.24) are given in Appendix A. Finally, we apply (3.24) to expression (3.23) to obtain a weak expression for the auxiliary variable:

$$\sum_{K_k}\int_{K_k}W_k(\Theta_k - TU_{4,k})\mathrm{d}K = -\sum_{K_k}\int_{K_k}W_k\mathscr{R}_k\mathrm{d}K. \tag{3.25}$$

As a result of the above manipulations in (3.25) and the arbitrariness of W_k, our aim to determine Θ_k has been reached. From (3.25), we find that

$$\Theta_k = TU_{4,k} - \mathscr{R}_k, \tag{3.26}$$

almost everywhere in Ω_{h}.

3.5. Primal formulation

The primal formulation can be obtained using the expression (3.25). Since $\nabla V_h \subset W_h$, the special case $W_k = (0,0,0,V_{4,k})$ can be considered in (3.25), and the auxiliary variable Θ can be replaced in the element integral of (3.19). Therefore,

$$\sum_{K_k}\int_{K_k}V_{4,k}\Theta_k\mathrm{d}K = \sum_{K_k}\int_{K_k}V_{4,k}(TU_{4,k} - \mathscr{R}_k)\mathrm{d}K. \tag{3.27}$$

The element boundary terms in (3.19) can be treated as follows:

$$\begin{aligned}\sum_{K_k}\int_{\partial K}V_i^{\mathsf{L}}\delta_{i4}\Theta_k^{\mathsf{L}}n_k^{\mathsf{L}}\mathrm{d}\mathscr{S} &= \sum_{\mathscr{S}\in\mathscr{S}_{\mathrm{I}}}\delta_{i4}\int_{\mathscr{S}}[\![V_i\Theta_k]\!]_k\mathrm{d}\mathscr{S} + \sum_{\mathscr{S}\in\mathscr{S}_{\mathrm{B}}}\delta_{i4}\int_{\mathscr{S}}V_i^{\mathsf{L}}\Theta_k^{\mathsf{L}}n_k^{\mathsf{L}}\mathrm{d}\mathscr{S}\\ &= \sum_{\mathscr{S}\in\mathscr{S}_{\mathrm{I}}}\delta_{i4}\int_{\mathscr{S}}\{\!\{V_i\}\!\}[\![\Theta_k]\!]_k + [\![V_i]\!]_k\{\!\{\Theta_k\}\!\}\mathrm{d}\mathscr{S} + \sum_{\mathscr{S}\in\mathscr{S}_{\mathrm{B}}}\delta_{i4}\int_{\mathscr{S}}V_i^{\mathsf{L}}\Theta_k^{\mathsf{L}}n_k^{\mathsf{L}}\mathrm{d}\mathscr{S} \qquad (3.28)\\ &= \sum_{\mathscr{S}\in\mathscr{S}_{\mathrm{I}}}\delta_{i4}\int_{\mathscr{S}}[\![V_i]\!]_k\{\!\{\Theta_k\}\!\}\mathrm{d}\mathscr{S} + \sum_{\mathscr{S}\in\mathscr{S}_{\mathrm{B}}}\delta_{i4}\int_{\mathscr{S}}V_i^{\mathsf{L}}\Theta_k^{\mathsf{L}}n_k^{\mathsf{L}}\mathrm{d}\mathscr{S}, \qquad (3.29)\end{aligned}$$

where we used relations (3.16) and (3.17) and invoked continuity of the flux such that $[\![\Theta_k]\!]_k = 0$ on internal faces. The average $\{\!\{\Theta_k\}\!\}$ is defined as

$$\{\!\{\Theta_k\}\!\} = \begin{cases}\{\!\{TU_{4,k} - \eta\mathscr{R}_k^{\mathscr{S}}\}\!\} & \text{on } \mathscr{S}_{\mathrm{I}},\\ T^BU_{4,k}^B - \eta\mathscr{R}_k^{\mathscr{S}} & \text{on } \mathscr{S}_{\mathrm{B}},\end{cases} \tag{3.30}$$

where, to reduce the width of the stencil, a *local lifting operator* $\mathscr{R}_k^{\mathscr{S}}$ was introduced satisfying

$$\sum_{K_k}\int_{K_k} W_k\mathscr{R}_k^{\mathscr{S}}\,\mathrm{d}K=\begin{cases}\int_{\mathscr{S}}\{\!\{TW_k\}\!\}[\![U_4]\!]_k\,\mathrm{d}\mathscr{S} & \text{on } \mathscr{S}_{\mathrm{I}},\\ \int_{\mathscr{S}} W_k^{\mathsf{L}}T^{\mathsf{L}}(U_4^{\mathsf{L}}-U_4^{B})n_k^{\mathsf{L}}\,\mathrm{d}\mathscr{S} & \text{on } \mathscr{S}_{\mathrm{B}}\end{cases} \tag{3.31}$$

for all $W_k\in W_h$ with $\eta>0$ a stabilization constant. In all simulations we use $\eta=4$.

Substitution of (3.26), (3.29) and (3.30) into (3.19) yields the final weak formulation

$$\begin{aligned}&\sum_{K_k}\int_{K_k}(V_iA_{ir}\partial_tU_r-V_{i,k}F_{ik}+V_iG_{ikr}U_{r,k}\\&\quad+V_{i,k}\delta_{i4}(TU_{4,k}-\mathscr{R}_k)-V_iS_i)\mathrm{d}K\\&\quad+\sum_{\mathscr{S}}\int_{\mathscr{S}}\Bigg((V_i^{\mathsf{L}}-V_i^{\mathsf{R}})(\{\!\{F_{ik}\}\!\}n_k^{\mathsf{L}}+\widetilde{H}_i^{\mathrm{nc}})\\&\quad+\{\!\{V_i\}\!\}\int_0^1 G_{ikr}(\phi(\tau;U^{\mathsf{L}},U^{\mathsf{R}}))\frac{\partial\phi_r}{\partial\tau}(\tau;U^{\mathsf{L}},U^{\mathsf{R}})\mathrm{d}\tau n_k^{\mathsf{L}}\Bigg)\mathrm{d}\mathscr{S}\\&\quad-\sum_{S\in\mathscr{S}_{\mathrm{I}}}\int_{\mathscr{S}}\delta_{i4}[\![V_i]\!]_k\{\!\{TU_{4,k}-\eta\mathscr{R}_k^{\mathscr{S}}\}\!\}\mathrm{d}\mathscr{S}\\&\quad-\sum_{S\in\mathscr{S}_{\mathrm{B}}}\int_{\mathscr{S}}\delta_{i4}V_i^{\mathsf{L}}(T^{B}U_{4,k}^{B}-\eta\mathscr{R}_k^{\mathscr{S}})n_k^{\mathsf{L}}\mathrm{d}\mathscr{S}=0.\end{aligned} \tag{3.32}$$

For conservative systems, the flux $(\{\!\{F_{ik}\}\!\}n_k^{\mathsf{L}}+\widetilde{H}_i^{\mathrm{nc}})$ is usually combined into one conservative, numerical flux at the element faces, such as the HLLC flux used before in [1] for the hydrodynamic part.

The non-conservative stabilizing flux vector $\widetilde{H}_i^{\mathrm{nc}}(U^{\mathsf{L}},U^{\mathsf{R}},n_k^{\mathsf{L}})$ follows from Rhebergen et al. [2] as

$$\widetilde{H}_i^{\mathrm{nc}}=\begin{cases}\frac{1}{2}[\![F_{ik}]\!]_k+\frac{1}{2}\int_0^1 G_{ikr}(\phi(\tau;U^{\mathsf{R}},U^{\mathsf{L}}))\frac{\partial\phi_r}{\partial\tau}(\tau;U^{\mathsf{R}},U^{\mathsf{L}})\mathrm{d}\tau n_k^{\mathsf{L}}\\ \quad\text{if } S_{\mathsf{L}}>0,\\ \frac{1}{2}(S_{\mathsf{R}}\overline{U}_i^{*}+S_{\mathsf{L}}\overline{U}_i^{*}-S_{\mathsf{L}}U_i^{\mathsf{L}}-S_{\mathsf{R}}U_i^{\mathsf{R}}),\quad\text{if } S_{\mathsf{L}}<0<S_{\mathsf{R}},\\ -\frac{1}{2}[\![F_{ik}]\!]_k+\frac{1}{2}\int_0^1 G_{ikr}(\phi(\tau;U^{\mathsf{L}},U^{\mathsf{R}}))\frac{\partial\phi_r}{\partial\tau}(\tau;U^{\mathsf{L}},U^{\mathsf{R}})\mathrm{d}\tau n_k^{\mathsf{L}},\\ \quad\text{if } S_{\mathsf{R}}<0.\end{cases} \tag{3.33}$$

The expression for the star state solution $\overline{U}_i^{*}$ in (3.33) is

$$\begin{aligned}\overline{U}_i^{*}=&\frac{S_{\mathsf{R}}U_i^{\mathsf{R}}-S_{\mathsf{L}}U_i^{\mathsf{L}}+(F_{ik}^{\mathsf{L}}-F_{ik}^{\mathsf{R}})n_k^{\mathsf{L}}}{S_{\mathsf{R}}-S_{\mathsf{L}}}-\frac{1}{S_{\mathsf{R}}-S_{\mathsf{L}}}\\&\times\int_0^1 G_{ikr}(\phi(\tau;U^{\mathsf{L}},U^{\mathsf{R}}))\frac{\partial\phi_r}{\partial\tau}(\tau;U^{\mathsf{L}},U^{\mathsf{R}})\mathrm{d}\tau n_k^{\mathsf{L}}.\end{aligned} \tag{3.34}$$

The left and right wave speeds are S_{L} and S_{R}, respectively. These are determined by taking the smallest and largest of the (approximate) four real eigenvalues of the hyperbolic part of the system (2.7). The eigenvalues used follow from the matrix $(\partial F_{ik}/\partial U_r+G_{ikr})n_k^{\mathsf{L}}$ for the case $\epsilon=1$ valid in (pseudo-)time, see §3.6. The hyperbolic part of the corresponding system in the direction $\hat{x}$ normal to a face can be written as

$$\begin{aligned}&\partial_t(hu)+\partial_{\hat{x}}(huq+\mathsf{F}^{-2}h^2n_x/2)+\mathsf{F}^{-2}hn_x\partial_{\hat{x}}b=0,\\&\partial_t(hv)+\partial_{\hat{x}}(hvq+\mathsf{F}^{-2}h^2n_y/2)+\mathsf{F}^{-2}hn_y\partial_{\hat{x}}b=0,\\&\partial_th+\partial_{\hat{x}}(hq)=0,\quad\partial_tb+\partial_{\hat{x}}(|\mathbf{u}|^{\beta-1}q)=0\end{aligned} \tag{3.35}$$

with $q=n_xu+n_yv$ and $n_k^{\mathsf{L}}=(n_x,n_y)^{\mathrm{T}}$. For the eigenvalue analysis it is easier to rewrite (3.35) as

$$\begin{aligned}&\partial_th+\partial_{\hat{x}}(hq)=0,\quad\partial_tu+q\partial_{\hat{x}}u+\mathsf{F}^{-2}n_x\partial_{\hat{x}}(h+b)=0,\\&\partial_tb+\partial_{\hat{x}}(|\mathbf{u}|^{\beta-1}q)=0,\quad\partial_tv+q\partial_{\hat{x}}v+\mathsf{F}^{-2}n_y\partial_{\hat{x}}(h+b)=0.\end{aligned} \tag{3.36}$$

The approximate eigenvalues λ corresponding to the system (3.36) follow from the polynomial

$$\begin{aligned}0&=\begin{vmatrix}q-\lambda & hn_x & hn_y & 0\\ \mathsf{F}^{-2}n_x & q-\lambda & 0 & \mathsf{F}^{-2}n_x\\ \mathsf{F}^{-2}n_y & 0 & q-\lambda & \mathsf{F}^{-2}n_y\\ 0 & n_xd & n_yd & -\lambda\end{vmatrix}\\&=(\lambda-q)(\lambda^3-2q\lambda^2+\lambda(q^2-\mathsf{F}^{-2}(d+h))+\mathsf{F}^{-2}qd)\end{aligned} \tag{3.37}$$

with approximation $d=\beta|\mathbf{u}|^{\beta-1}$ based on the one-dimensional problem, cf. [15]. In the one-dimensional case, $q=u$, the eigenvalue $\lambda=q$ is absent and $d=\beta q^{\beta-1}$. We emphasize that the following eigenvalues calculated are classical, exact solutions to the above quartic polynomial, which itself is an approximation of the matrix associated with system (3.36). The cubic polynomial has real eigenvalues provided its determinant $D=Q^3+R^2<0$ with

$$\begin{aligned}R&=\frac{-18q(-\mathsf{F}^{-2}(h+d)+q^2)-27\mathsf{F}^{-2}qd+16q^3}{54},\\Q&=-\frac{q^2+3\mathsf{F}^{-2}(h+d)}{9},\end{aligned} \tag{3.38}$$

and after some algebra we find that $D<0$.

The four eigenvalues are

$$\begin{aligned}&\lambda=q,\quad\lambda=2\sqrt{-Q}\cos(\theta/3)+2q/3,\\&\lambda=2\sqrt{-Q}\cos(\theta/3+2\pi/3)+2q/3\quad\text{and}\\&\lambda=2\sqrt{-Q}\cos(\theta/3+4\pi/3)+2q/3,\end{aligned} \tag{3.39}$$

with $\theta=\cos^{-1}(R/\sqrt{-Q^3})$. It is also possible to calculate the exact eigenvalues of the system but at great computational expense. The evaluation of the above approximate eigenvalues turns out to be so efficient that further simplification is unnecessary. Finally, the algebraic system corresponding to the weak formulation (3.32) and details on the global and local lifting operators $\mathscr{R}_k$ and $\mathscr{R}_k^{\mathscr{S}}$ defined in (3.24) and (3.31) are given in Appendix A.

The numerical flux in the weak formulation (3.32)–(3.34) reduces to the HLL numerical flux when the topography is constant. Rest flow stays at rest even for variable bottom topography as was shown in [2].

3.6. Time stepping method and solver

A time discretization is required to solve the ordinary differential equations that emerge from the spatial finite

element discretization. Numerical complications may arise due to the presence of a small parameter ϵ in front of the time derivatives in the depth and momentum equations. However, at leading order, in the limit $\epsilon \to 0$ a coupled differential–algebraic system emerges. We therefore derive a new time stepping scheme for solving the system in the limit $\epsilon \to 0$ next.

Consider first the continuum system (2.7a)–(2.7c) extended with a fast, hydrodynamic time scale $\tau = t/\epsilon$ such that $\partial_t \to \partial_\tau/\epsilon + \partial_t$. Dependencies then become $h = h(\mathbf{x}, t, \tau)$ and so forth. The resulting extended system reads

$$\partial_\tau h + \epsilon\partial_t h + \nabla\cdot(h\mathbf{u}) = 0, \tag{3.40a}$$

$$\partial_\tau(h\mathbf{u}) + \epsilon\partial_t(h\mathbf{u}) + \nabla\cdot(h\mathbf{u}\mathbf{u}) + \mathsf{F}^{-2}\nabla(h^2/2) = -\mathsf{F}^{-2}h\nabla b - C_\mathrm{f}\mathbf{u}|\mathbf{u}|, \tag{3.40b}$$

$$\partial_\tau b/\epsilon + \partial_t b + \nabla\cdot\mathbf{q}_\mathrm{b} = 0 \tag{3.40c}$$

together with (2.7d). This extension, albeit more complicated than the actual system of interest, is more amenable to asymptotic analysis. The variables $h, h\mathbf{u}$ and b as functions of $\{\mathbf{x}, t, \tau\}$ are expanded in a perturbation series in ϵ

$$\begin{aligned} h(\mathbf{x},t,\tau) &= h^{(0)}(\mathbf{x},t,\tau) + \epsilon h^{(1)}(\mathbf{x},t,\tau) + \mathcal{O}(\epsilon^2),\\ \mathbf{u}(\mathbf{x},t,\tau) &= \mathbf{u}^{(0)}(\mathbf{x},t,\tau) + \epsilon \mathbf{u}^{(1)}(\mathbf{x},t,\tau) + \mathcal{O}(\epsilon^2),\\ b(\mathbf{x},t,\tau) &= b^{(0)}(\mathbf{x},t,\tau) + \epsilon b^{(1)}(\mathbf{x},t,\tau) + \mathcal{O}(\epsilon^2) \end{aligned} \tag{3.41}$$

with $\mathcal{O}(\epsilon^2)$ denoting terms of order ϵ^2 or higher. Next, we substitute (3.41) into (3.40) and evaluate the result at leading order in ϵ.

At leading order, $\mathcal{O}(1/\epsilon)$ in the sediment equation (3.40c), we find that $\partial_\tau b^{(0)} = 0$ such that $b^{(0)} = b^{(0)}(\mathbf{x}, t)$ is independent of the fast time scale. At $\mathcal{O}(1)$, we therefore have

$$\partial_\tau h^{(0)} + \nabla\cdot(h^{(0)}\mathbf{u}^{(0)}) = 0, \tag{3.42a}$$

$$\partial_\tau(h^{(0)}\mathbf{u}^{(0)}) + \nabla\cdot(h^{(0)}\mathbf{u}^{(0)}\mathbf{u}^{(0)}) + \mathsf{F}^{-2}\nabla({h^{(0)}}^2/2) = -\mathsf{F}^{-2}h^{(0)}\nabla b^{(0)} - C_\mathrm{f}\mathbf{u}^{(0)}|\mathbf{u}^{(0)}|, \tag{3.42b}$$

$$\partial_\tau b^{(1)} + \partial_t b^{(0)} + \nabla\cdot(|\mathbf{u}^{(0)}|^\beta(\mathbf{u}^{(0)}/|\mathbf{u}^{(0)}| - \kappa\nabla b^{(0)})) = 0 \tag{3.42c}$$

in which $h^{(0)}$ and $\mathbf{u}^{(0)}$ depend on $\mathbf{x}, t$ and τ; but $b^{(0)}$ only on $\mathbf{x}$ and t.

To avoid secular growth, the sediment transport equation (3.42c) is averaged over the fast time scale to obtain

$$\partial_t b^{(0)} + \nabla\cdot(\langle|\mathbf{u}^{(0)}|^{\beta-1}\mathbf{u}^{(0)}\rangle - \langle|\mathbf{u}^{(0)}|^\beta\rangle\kappa\nabla b^{(0)}) = 0, \tag{3.43}$$

where $\langle\cdot\rangle$ denotes the fast time averaging. Eqs. (3.42a) and (3.42b) only depend parametrically on the slow, sediment time scale t for example through $b^{(0)}(\mathbf{x}, t)$ as no slow time derivatives ∂_t appear. If we therefore solve $h^{(0)}$ and $\mathbf{u}^{(0)}$ in (3.42a) and (3.42b) first, in particular on the fast time scale, we can subsequently use it in the averaged Eq. (3.43). If the long-time fast average is constant on the fast time scale τ, the stationary fast time solution dominates and we have actually solved the original system for the case $\epsilon = 0$. For (rapidly) oscillating boundary data, no stationary solution may exist, in which case the averaging is required.

A leading-order numerical approach, for the stationary hydrodynamic solutions in the limit $\Delta t \to 0$ (e.g., system (2.7) with $\epsilon = 0$), is therefore to solve the discrete hydrodynamic continuity and momentum equations on the fast time scale τ till stationarity is reached. The discretization of $b(\mathbf{x}, t)$ is then fixed on the fast time scale, and the discretized sediment equation is subsequently solved separately. We intertwine a fifth-order Runge–Kutta scheme for the fast or pseudo-time τ for the mass and momentum equations, designed to be a dissipative time integration scheme to efficiently reach the steady-state in pseudo-time in [16], and an accurate explicit time discretization for the sediment equation (the third order Runge–Kutta scheme used in [17,1]). Another approach is to calculate the steady hydrodynamic state first, and use the corresponding velocity in the sediment equation, to be solved subsequently. We also used this separate approach with success but it is formerly only first order in time because one then only uses the previous, old value of the velocity in the sediment equation also at the intermediate steps, or, vice versa, one only uses the previous, old value of b in the hydrodynamic equations and not at the intermediate time values of b. The intertwined time stepping schemes guarantee the third-order accuracy in time used in the sediment equation provided a steady-state criterion is reached for the hydrodynamics. We considered the steady hydrodynamic state to be achieved when the residue is smaller than 10^{-5}, following the approach in [16]; the residue is defined here as the entire steady space discontinuous Galerkin finite element discretization for the hydrodynamics. Further details are relegated to Appendix A.4.

Besides the space DGFEM, we also applied and extended the space–time DGFEM, developed in [2] for hyperbolic systems with non-conservative products, to our morphodynamic system. In all verifications with $\kappa = 0$ the space and space–time DGFEM's have been compared, successfully. Local artificial friction was only required for the test case in section 4.2. This slope limiter was only introduced when the jumps of certain variables across faces were too large, cf. [20,16].

4. Verification

In this section, the accuracy of our numerical scheme, for (2.7) with $\epsilon = 0$, is demonstrated by several test cases, also in comparison with exact solutions. In the following test cases, we use linear polynomials yielding formal second-order accuracy in space. The time stepping scheme is second- and third-order for the space–time and space discontinuous finite element discretizations, respectively.

4.1. Evolution of an isolated bedform

Consider the evolution of an initially symmetric, isolated bedform subject to steady, unidirectional flow in a

domain $x \in [0,1]$. The setup consists of a channel with a small, but finite amplitude perturbation of the bed level initially centered at x_p, with amplitude A and width $2d$:

$$b(x,0) = \begin{cases} A - A\cos\left(\frac{\pi}{d}(x - x_p + d)\right), & \text{if } |(x - x_p)| \leqslant d, \\ 0.0, & \text{otherwise,} \end{cases} \tag{4.1}$$

where $A = 0.05, d = 0.1$ and $x_p = 0.5$. At the left boundary we set $h = h(x \downarrow 0, t)$, $hu = 1$, and $b = 0$, and at the right boundary $h = 1, hu = hu(x \uparrow 1, t)$, and $b = 0$. As initial condition, the water surface elevation $h(x,0) + b(x,0) = 1$ and flow velocity $u(x,0) = 1$. For this test we adopt $\beta = 3, \mathsf{F} = 0.1$, and $C_\mathrm{f} = 0.0$. In Fig. 1, we show the evolution of the solution with $\kappa = 0.0$, computed from time $t = 0.0$ to $t = 0.04$. Fig. 2 shows the initial condition and the exact and numerical solutions of the isolated bedform computed at time 0.04. Table 1 shows that the scheme is second-order accurate by computing the L^2 and L^∞ norms of the numerical error in b with respect to the exact solution. In comparison, both space and space–time DGFEM's converge and agree with one another. Fig. 3 shows the evolution of the isolated bedform with $\kappa = 0.01$ and $\kappa = 0.1$, respectively.

This exact solution for $\kappa = 0$, used in Table 1, is derived as follows. In the limit $\epsilon \to 0$ and $\kappa \to 0$ on the slow time scale and in one spatial dimension, the system (2.7a)–(2.7d) satisfies

$$\partial_x(hu) = 0, \tag{4.2a}$$

$$\partial_x\left(hu^2 + \frac{1}{2}\mathsf{F}^{-2}h^2\right) = -\mathsf{F}^{-2}h\partial_x b - C_\mathrm{f}|u|u, \tag{4.2b}$$

$$\partial_t b + \partial_x(|u|^{\beta-1}u) = 0. \tag{4.2c}$$

For $C_\mathrm{f} = 0$ and by using upstream values u_0, b_0 and h_0 with discharge $Q = h_0u_0$ and Bernoulli constant $B_0 = u_0^2/2 + \mathsf{F}^{-2}(h_0 + b_0)$, this system reduces to

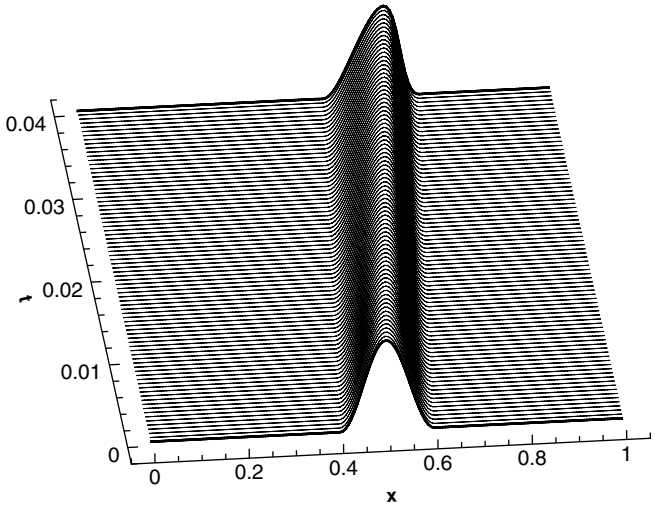

Fig. 1. Evolution of an isolated bedform from time $t = 0.0$ to 0.04 with $\kappa = 0.0$ using a mesh of 160 elements.

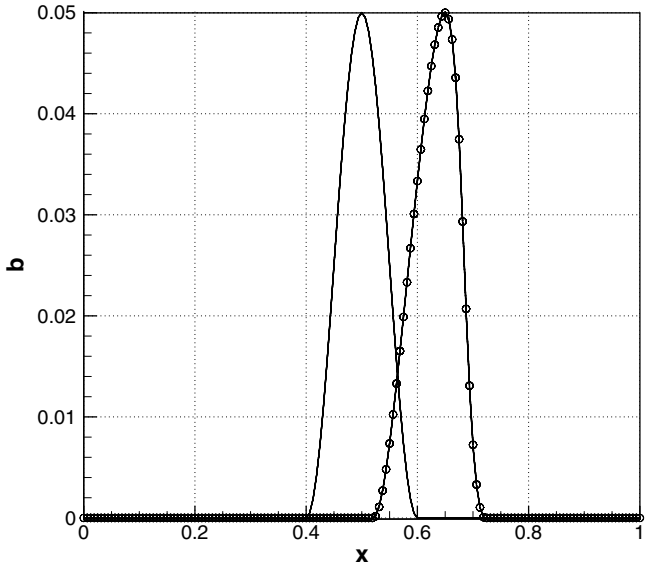

Fig. 2. Exact (circle) and DGFEM numerical simulation (solid line) with $\kappa = 0.0$.

$$\frac{1}{2}u^3 + (\mathsf{F}^{-2}b - B_0)u + \mathsf{F}^{-2}Q = 0, \quad h = Q/u \tag{4.3}$$

in which we consider flows with a subcritical root $u = u(b)$ as solution. Substitution of (4.3) into the sediment equation in (4.2c) then yields a conservation law in the variable b. Further manipulation gives

$$\partial_t b + \beta|u(b)|^{\beta-1}\frac{\partial u(b)}{\partial b}\partial_x b = 0, \tag{4.4}$$

which has the following implicit solution till the time of wave breaking:

$$\begin{aligned} &x = x_i + \lambda(b)t, \quad b = b_i(x_i) \text{ or} \\ &b = b_i(x - \lambda(b)t) \quad \text{with } \lambda(b) = \tfrac{\beta|u(b)|^{\beta-1}\mathsf{F}^{-2}u(b)}{\mathsf{F}^{-2}Q/u(b) - u(b)^2}. \end{aligned} \tag{4.5}$$

4.2. Graded river

In this test, the dynamics induced by a sudden overload of sediment to a base flow solution is considered in a straight channel with unitary width. The exact base state flow solution is given by $\mathbf{u}_0 = (u_0, v_0)^\mathrm{T} = (u_0, 0)^\mathrm{T} = (1,0)^\mathrm{T}, h_0 = 1$, $\mathbf{q}_\mathrm{b} = (q_\mathrm{b}^0, 0)^\mathrm{T} = (1,0)^\mathrm{T}$. Assuming a bed slope $S_0 = 0.0001$, Froude number $\mathsf{F} = 0.1$, and $\kappa = 0.0$, the base state leads to the relation $C_\mathrm{f} = S_0\mathsf{F}^{-2} = 0.01$. The *aggradation* of the channel starts when an increase of the bottom topography $b(0,t) = b(0,0) + \delta$ for $t > 0$ is considered at the beginning of the inlet, here with $\delta = 0.0012$. For this test we consider a domain $x \in [0,5]$ divided into 80 cells. At the left boundary we set $h = h(x \downarrow 0, t), hu = 1$, and $b = 0.0012$ and for the right boundary $h = 1, hu = hu(x \uparrow 5, t)$, and $b = -0.0005$. As initial condition, the water depth $h(x,0) = 1$, the flow velocity $u(x,0) = 1$, and the bottom elevation has a constant bed slope S_0. Fig. 4 shows the evolution of the bottom topogra-

Table 1
The L^2 and L^∞ error norm of bottom level b and convergence rates with order p for the space and space–time DG solutions

N	Space DG				Space–time DG			
	L_2 error	p	L_∞ error	p	L_2 error	p	L_∞ error	p
40	8.7626e−04		4.2634e−03		1.0006e−03		4.1827e−03	
80	2.1120e−04	2.1	1.1714e−03	1.9	1.5085e−04	2.8	9.5121e−04	2.1
160	4.9064e−05	2.1	2.7252e−04	2.1	3.6876e−05	2.0	1.9613e−04	2.3
320	1.1558e−05	2.1	5.9797e−05	2.2	9.4587e−06	2.0	4.5131e−05	2.1

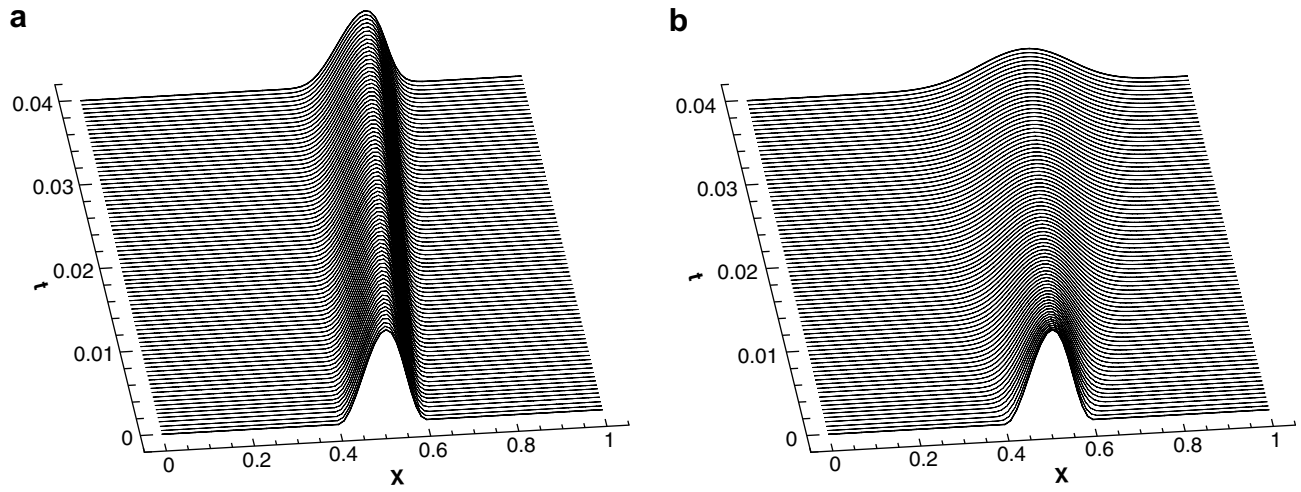

Fig. 3. Evolution of an isolated bedform from time $t = 0.0$ to 0.04 for (a) $\kappa = 0.010$ and (b) $\kappa = 0.1$, both using a mesh of 80 elements.

phy and the water depth from time $t = 0.0$ to 1.4. For this test, we compute the solution with space and space–time DG discretizations, obtaining the same, good results. The evolution of the bed level from time $t = 0.0$ to $t = 1.4$ with $\kappa = 0.1$ is shown in Fig. 5.

4.3. Travelling wave solution

In this test, a travelling sediment wave is examined in detail to assess the discretization of the downslope gravitational term present in the bed evolution equation. Assuming unidirectional and one-dimensional flow, travelling wave solutions [18] can be found after substituting $b = b(\xi)$ into (2.7a)–(2.7d) for $\epsilon = 0$ and $\xi = x - ct$ to obtain

$$b' = (-cb + u^\beta - \mathcal{Q})/\kappa u^\beta \tag{4.6}$$

with $b' = \partial_\xi b$, c the wave speed, $\mathcal{Q}$ the integration constant, and $u = u(b)$ the flow velocity, i.e., the subcritical root of the stationary hydrodynamic equations (4.3). Eq. (4.6) is

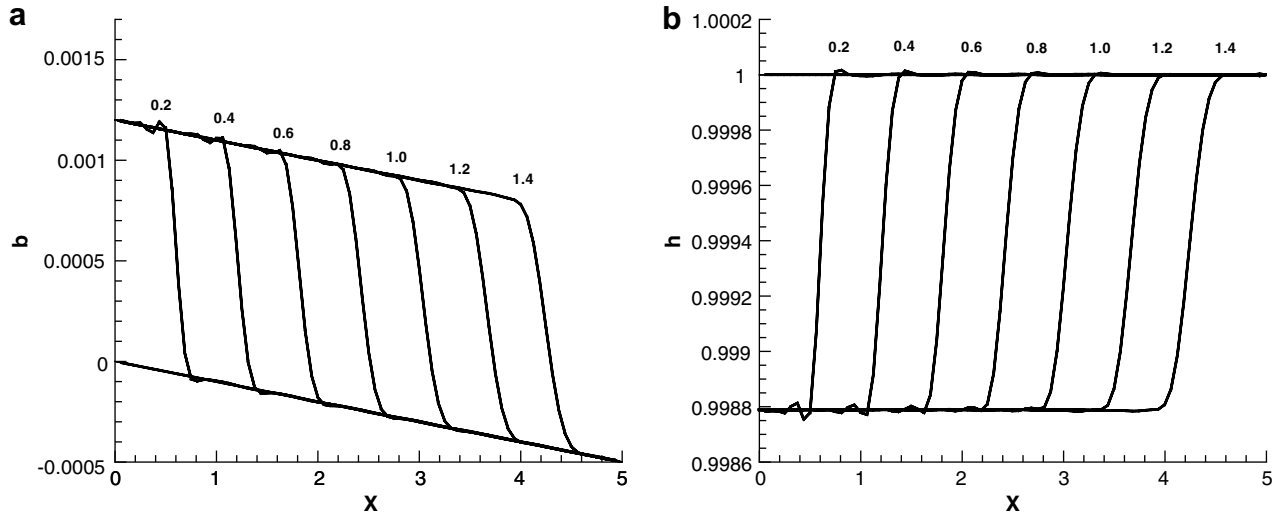

Fig. 4. Profiles of (a) bottom level $b(x)$ and (b) water depth $h(x)$ in a straight channel from time $t = 0.0$ to $t = 1.4$ with $\kappa = 0.0$.

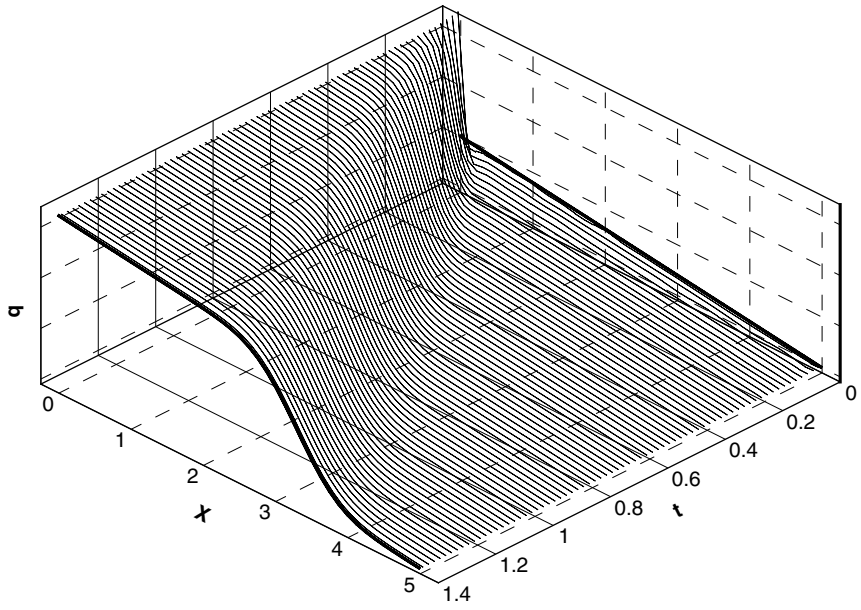

Fig. 5. Evolution of the bottom level in a straight channel from time $t = 0.0$ to 1.4 with $\kappa = 0.1$.

solved using a fourth-order Runge–Kutta discretization for small $\Delta\xi$. For the simulations we use $\beta = 3, \kappa = 1, c = 1$, $Q = 1, \mathsf{F} = 0.1$, and $\mathscr{Q} = 1$. Fig. 6 shows the travelling wave DGFEM and the "exact" solution of (4.6) from time $t = 0$ to 8 in a domain $x \in [0, 5]$. Table 2 confirms the good, second-order accuracy of the discretization, including the primal formulation for the diffusive terms.

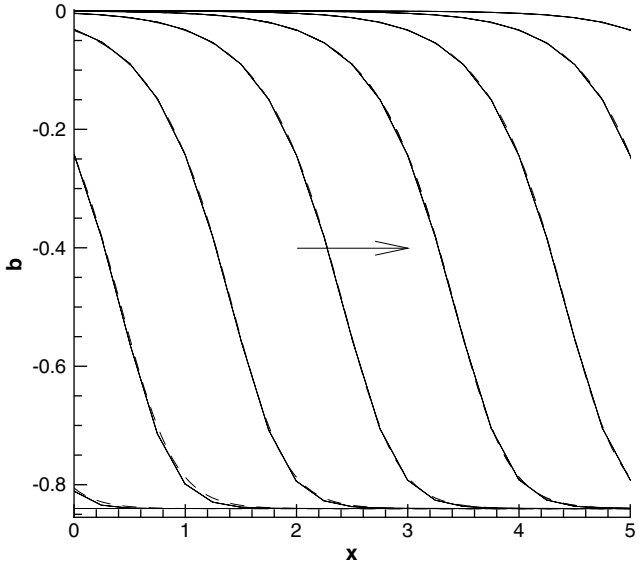

Fig. 6. DGFEM (solid) and "exact" solution of (4.6) (dashed) solutions of the test with a travelling sediment wave moving from left to right from time $t = 0$ to 8 using a mesh of 20 elements.

Table 2
The L^2 and L^∞ error norms of b and convergence rates with order p for the space DG solution

N	Space DG			
	L_2 error	p	L_∞ error	p
10	1.542e−01		1.460e−01	
20	3.840e−02	2.0	4.756e−02	1.6
40	8.278e−03	2.2	1.022e−02	2.2
80	2.151e−03	1.9	1.997e−03	2.3

5. Validation

The applicability of our numerical schemes is shown in two test cases: the evolution of a trench in a natural channel, and the hydraulic and sediment transport through a contraction.

5.1. Evolution of a trench in the Paraná river

A sub-fluvial tunnel underneath the Paraná river links the Santa Fe and Paraná cities in Argentina. During the flood of 1983, the tail of a 7 m high dune almost uncovered part of the tunnel, nearly leading to its collapse. Subsequently, as part of a study program aimed to further protect the underwater structure, a trench was dug in the main channel during the months of October–December of 1992 to analyze the bedload transport nearby the tunnel axis [14]. To test our DGFEM model, a comparison is made between observations and a numerical simulation of the evolution of the trench excavated in the main channel of the Paraná river.

For the numerical model, we used $\beta = 3$ and the Froude number $\mathsf{F} = 0.07950$ was computed based on the characteristic scales $h_0^* = l_0^* = 15.30$ m, and $q_0^* = u_0^* h_0^* = 14.9\ \mathrm{m^2\ s^{-1}}$. These hydrological estimates were taken from [14]. We chose $t_0^* = 22.5$ days and thus derive $\alpha^* = 1.31 \times 10^{-4}\ \mathrm{m^{2-\beta}/s^{1-\beta}}$ and $\epsilon = 8.1 \times 10^{-6}$, cf. Section 2.3. The latter flux ratio lies between the quoted values of 10^{-5} and

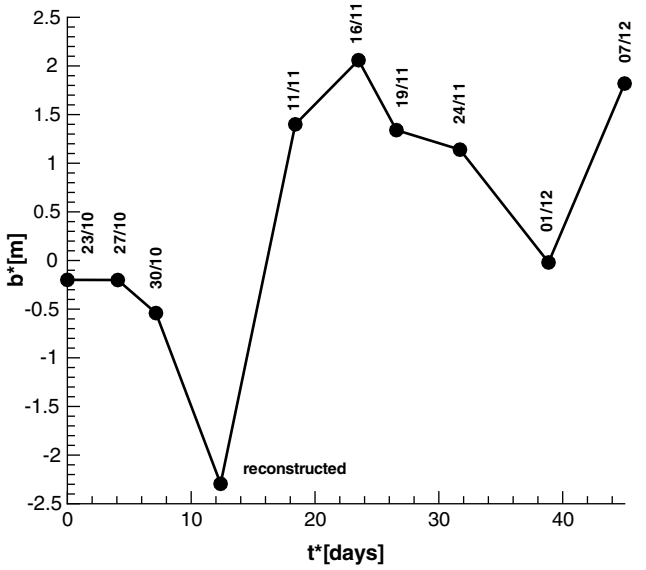

Fig. 7. Boundary conditions at the left boundary are determined from the data at the boundary and a reconstruction using interior values. To reconstruct the missing boundary data, the velocity of a dip was estimated and the minimum value of the topography was traced back to the left boundary. The missing data point seems so far from the available data due to a propagation of a depression in the bottom level entering the domain. This can be assessed by analyzing the field data, see Fig. 8.

10^{-6} in [14]. For the Paraná trench test case, the dimensional values are displayed in the figures, even though we compute them in dimensionless form.

In a domain $x \in [L_l, L_r]$, with $L_l = -19.6$ (circa -300 m) and $L_r = 5.18$ (circa 80 m); upstream boundary conditions are set to $h = h(x \downarrow L_l, t), hu = 1$, and $b = b(L_l, t)$ given by the measured and reconstructed values of the bed topography at the beginning of the trench. Between October 30th and November 11th, the missing data at the left boundary were estimated as shown in Fig. 7. Downstream boundary conditions are $h = 1, hu = hu(x \uparrow L_r, t)$, and $b = b(x \uparrow L_r, t)$. Initial water depth is $h(x, 0) = 1 - b(x, 0)$, and the initial velocity $u(x, 0)$ corresponds with the steady hydrodynamic results determined by the subcritical root $u(x, 0) = u(b(x, 0))$, see (4.3), with $b(x, 0)$ based on the topography field data measured on October 23rd, 1992. The value $\kappa = 0.45$ was chosen to match the measured data better. The simulation was performed for a period of 45 days and we present a comparison between measured and simulated profiles for October 23rd to December 7th 1992 in Fig. 8. Details of the profiles are shown in Fig. 9. Comparison of simulations with field data show that the main characteristics of the profile, such as the propagation speed of the large, localized step with a planar avalanche face spanning the width of the trench and the dip flowing into the domain, are well captured by our DGFEM simulations. At the end of the trench, extrapolated boundary conditions for $b(x, t)$ were assigned and a discrepancy between simulations and measurements is found for time $t > 1$ because of the coarse reconstruction of the missing field data at the entrance boundary.

5.2. Hydraulic and sediment transport through a contraction

Stationary hydraulic and sedimentary flows are considered through a channel with fixed vertical walls and a localized smooth contraction in the middle of the channel. The main reason to consider the bed evolution of hydraulic flow through contraction is to explore the bed evolution in this geometry with an eye to its potential for laboratory experiments. Furthermore, we compare our simulations with the

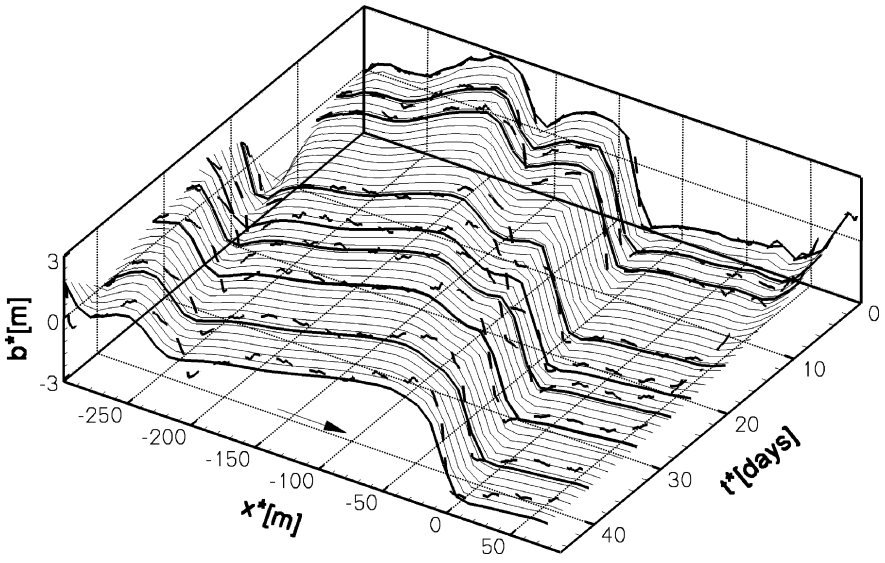

Fig. 8. Profiles of the numerical evolution of the bottom in a trench from October 23rd to December 7th 1992. Measured profiles (dashed or jagged lines) correspond to October 23rd, October 27th, October 30th, November 11st, November 16th, November 19th, December 1st, and December 7th. The arrow indicates the direction of the flow.

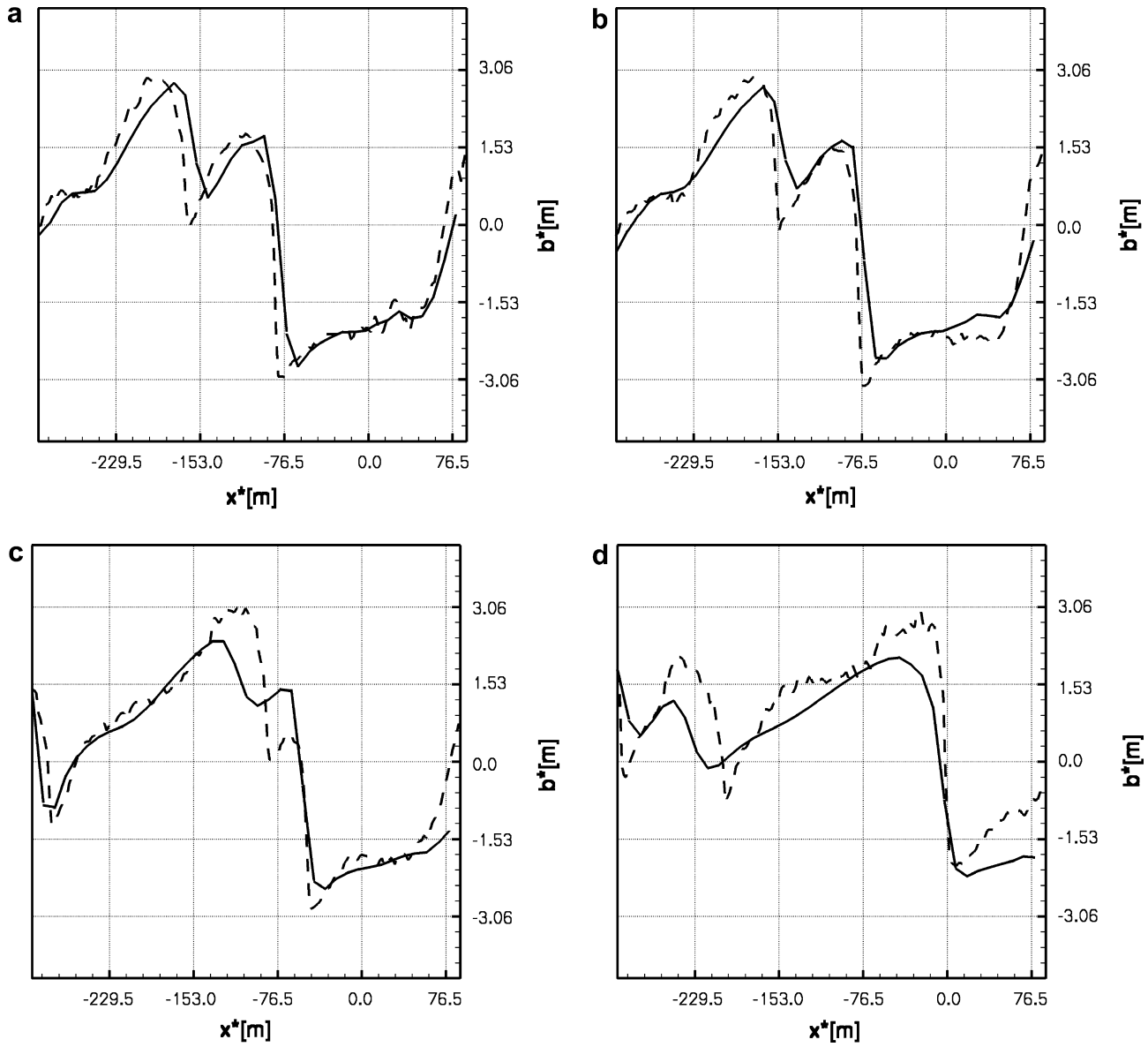

Fig. 9. Profiles of the numerical evolution of the bottom in a trench (measured: dashed or jagged lines); (a) October 27th; (b) October 30th; (c) November 11th; and (d) December 7th.

ones of Kubatko et al. [19]. Two-dimensional flow and sediment discharge simulations will be presented for two test cases. For the first case, we compare simulations for $\kappa = 0$ with an asymptotic solution based on cross-sectionally averaged equations solely depending on the downstream direction x and time t. The resulting variables are the mean velocity, the mean depth and the mean height of the topography. In the averaging procedure perturbations to these means are neglected as these will be small if the constriction is slowly varying in x and the channel sufficiently wide. The variations in flow scales across the channel are then small compared to the downstream scales of interest.

First, consider asymptotic solutions in a channel of varying width $r = r(x)$ with vertical walls. A cross-sectional average of the system (2.7) for $\kappa = 0$, while neglecting perturbations of mean quantities, leads to the following one-dimensional system:

$$\epsilon\partial_t(hr) + \partial_x(hru) = 0, \tag{5.1a}$$

$$\epsilon\partial_t(hru) + \partial_x\left(hru^2 + \frac{1}{2}\mathsf{F}^{-2}rh^2\right) = \frac{1}{2}\mathsf{F}^{-2}h^2\partial_x r - \mathsf{F}^{-2}hr\partial_x b - C_{\mathrm{f}}r|u|u, \tag{5.1b}$$

$$\partial_t(br) + \partial_x(r|u|^{\beta-1}u) = 0. \tag{5.1c}$$

Steady-state solutions of (5.1) are sought. These satisfy

$$\partial_x(hru) = 0, \tag{5.2a}$$

$$\partial_x\left(hru^2 + \frac{1}{2}\mathsf{F}^{-2}rh^2\right) = \frac{1}{2}\mathsf{F}^{-2}h^2\partial_x r - \mathsf{F}^{-2}hr\partial_x b - C_{\mathrm{f}}r|u|u, \tag{5.2b}$$

$$\partial_x(r|u|^{\beta-1}u) = 0 \tag{5.2c}$$

with unknowns $b = b(x), h = h(x), u = u(x)$ for a given channel width $r = r(x)$. After introducing a hydrodynamic discharge $Q = u_0 h_0 r_0$; sediment discharge rate $S_e = r u_0^\beta$; and upstream constant values u_0, h_0, r_0, b_0; the solution of (5.2) becomes

$$u(x) = \left(\frac{S_e}{r(x)}\right)^{1/\beta}, \quad h(x) = \frac{Q}{r(x)u(x)},$$
$$b(x) = b_0 + h_0 - h(x) + \mathrm{F}^2 \frac{1}{2}(u_0^2 - u(x)^2) - \mathrm{F}^2 \int_{x_0}^{x} \frac{C_\mathrm{f}|u(\tilde{x})|u(\tilde{x})}{h(\tilde{x})} \mathrm{d}\tilde{x} \tag{5.3}$$

with $x = x_0$ the entrance of the channel. Sample solutions for the case $\kappa = 0$ and $C_\mathrm{f} = 0$ and $C_\mathrm{f} > 0$ are displayed in Fig. 10(a,b). In the latter Fig. 10(b), we notice the graded river flow upstream of the contraction, as in Section 4.2.

Second, we consider the corresponding numerical test case. At the inflow boundary we set $h = h(\mathbf{x} \downarrow -5, t)$, $hu = 1, hv = 0$ and $b = 0$; and, for the outflow boundary $h = 1, hu = hu(\mathbf{x} \uparrow 5, t), hv = hv(\mathbf{x} \uparrow 5, t)$, and $b = 0$. Initial conditions for $h(\mathbf{x})$ and $b(\mathbf{x})$ are given by the asymptotic solution (5.3). A mesh of $(11 + 40 + 6) \times 10$ elements was

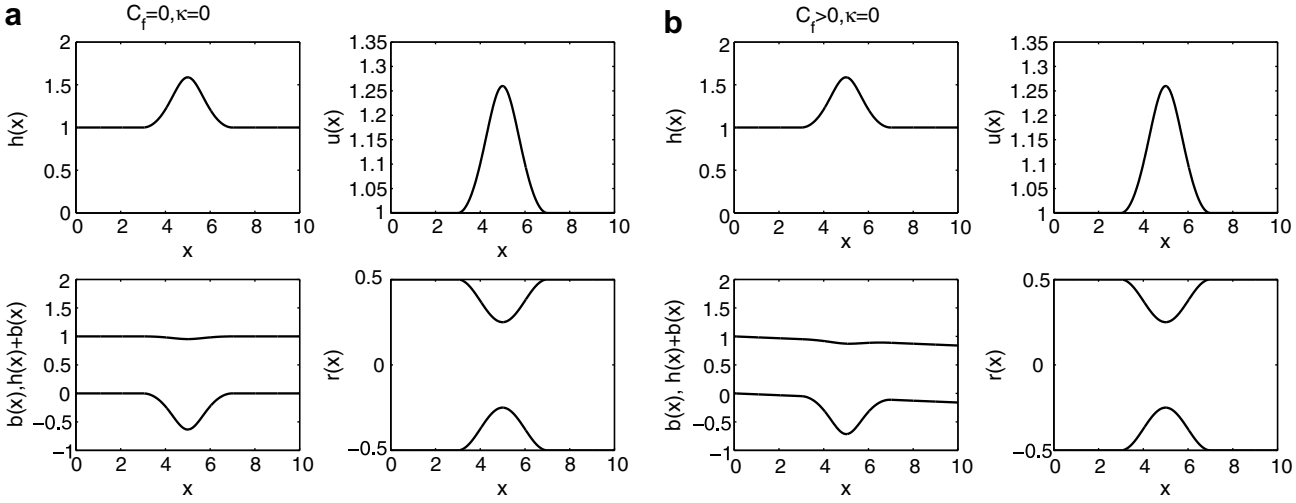

Fig. 10. Exact steady-state solutions of Eq. (5.2) for the mean velocity $u(x)$, mean depth $h(x)$ and mean bottom $b(x)$, averaged across the channel which has fixed, specified width $r(x)$. These are asymptotic solutions of the two-dimensional equations (2.7a)–(2.7d) for $\kappa = 0, \epsilon = 0$, and (a) $C_\mathrm{f} = 0$ and (b) $C_\mathrm{f} = 0.1$.

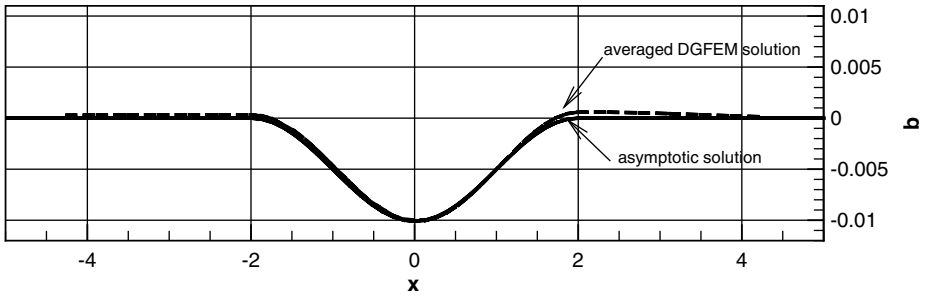

Fig. 11. Comparison between asymptotic (solid) and numerical simulation (dashed) for the bottom $b(x)$ averaged along the channel width for $\epsilon = 0, C_\mathrm{f} = 0$, and $\kappa = 0$. We used (5.3) with $Q = 1$, $\mathrm{F} = 0.1$, and $S_e = 1$.

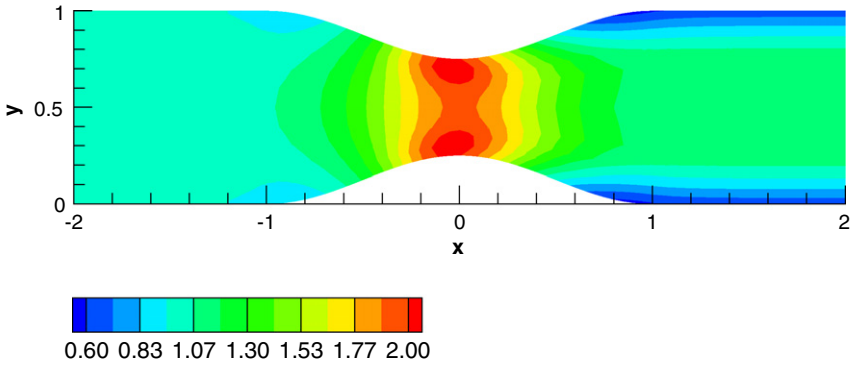

Fig. 12. Flow and sediment transport in a contraction channel: streamwise discharge $hu(\mathbf{x})$.

used in the inflow, contraction, and outflow region for both calculations with space and space–time discontinuous Galerkin finite element methods. In Fig. 11, we compare the asymptotic results against numerical simulation for the case $\kappa = 0$ and $C_f = 0$ assuming a constriction of 1% of the width of the channel. It can be seen that the numer-

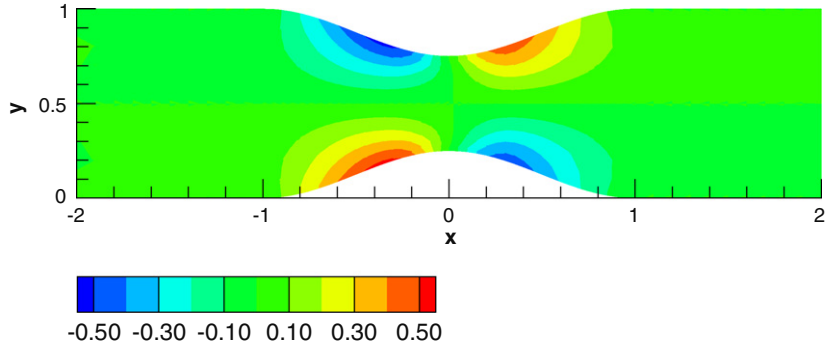

Fig. 13. Flow and sediment transport in a contraction channel: crosswise discharge $hv(\mathbf{x})$.

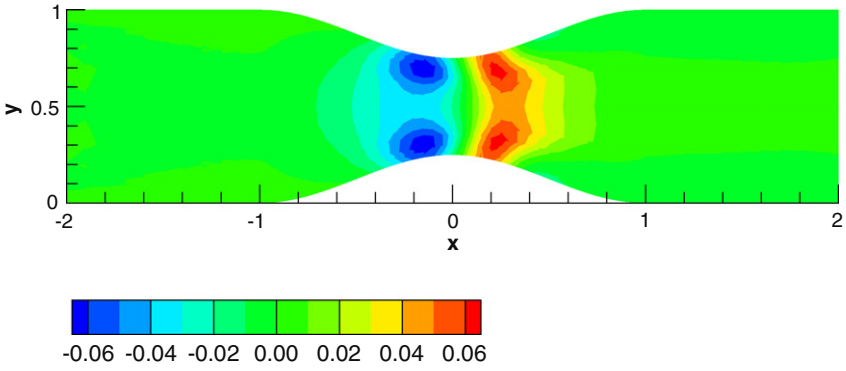

Fig. 14. Flow and sediment transport in a contraction channel: bottom profile $b(\mathbf{x})$.

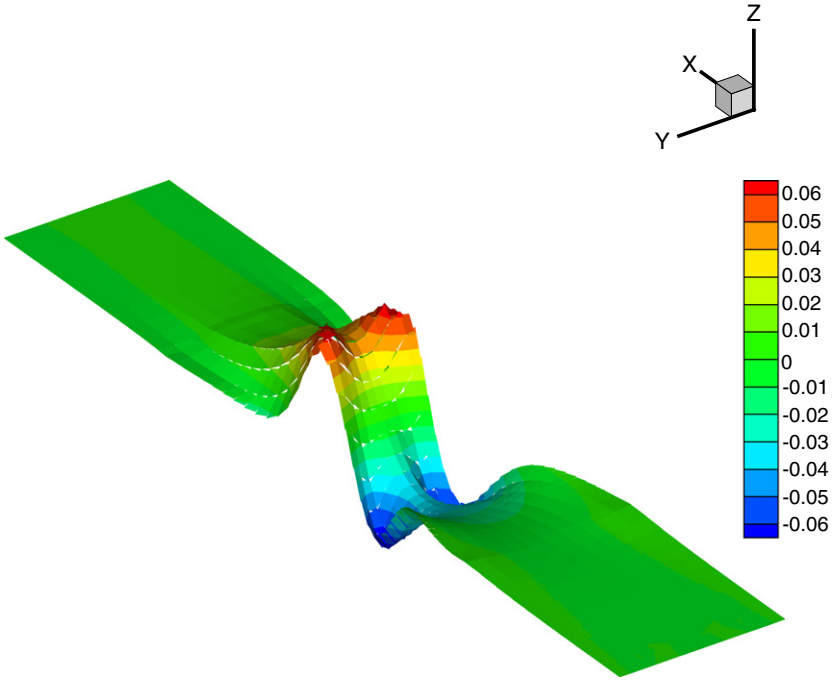

Fig. 15. Flow and sediment transport in a contraction channel: bottom profile $b(\mathbf{x})$.

ical and asymptotic solutions are highly similar, as expected.

Converging and diverging river channels can typically be found in nature. For the second validation, we examine the morphodynamic evolution of an initially flat bed channel in a converging channel [19]. Now, the constriction is 50% of the total width of the channel. At the inflow boundary, variables are set to $h = h(\mathbf{x} \downarrow -2, t), hu = 1, hv = 0$, and $b = 0$; and, at the outflow boundary $h = 1, hu = hu(\mathbf{x} \uparrow 2, t), hv = hv(\mathbf{x} \uparrow 2, t)$, and $b = 0$. Initial water depth and discharge correspond with the steady hydrodynamic results obtained with a preliminary simulation in which the bed is considered fixed and with $\mathsf{F} = 0.1$. Figs. 12–15 show the discharge $hu(\mathbf{x}), hv(\mathbf{x})$, and bed elevation $b(\mathbf{x})$ at time $t = 0.005$, respectively. As observed in [19], the bed experiences erosion in the converging part of the channel due to an increase in the flow velocity and the development of a mound in the diverging part of the channel, see Figs. 14 and 15; it is a product of a decreasing velocity, see Figs. 12 and 13. In the simulation, the water surface remains rather flat $h(\mathbf{x}) + b(\mathbf{x}) \approx 1$ as expected for low Froude numbers. Our results compare qualitatively well with those presented in [19], and are in good agreement with alternative simulations using the space–time DGFEM, cf. [20]. Laboratory experiments based on the proposed geometry are of further interest to validate these numerical results.

The CPU times for the space and space–time discontinuous Galerkin finite element methods were 5 and 17 h, respectively. Both codes were not optimized. The space–time code was a test code used for checking set up for calculations in four dimensions; here we used only one element and zero flux in the fourth direction (doubling the load). Major speed improvement of the space–time code can be obtained by employing multigrid methods [16], which are under development in our hpGEM software environment [21].

6. Conclusions

In this paper, we applied the discontinuous Galerkin finite element discretization of [2], concerning hyperbolic systems with non-conservative products, to a morphodynamic model for shallow flows over varying bottom topography. It is a system of coupled hyperbolic–parabolic equations. The computation time is greatly reduced by a hybrid approach with both conservative and intrinsically non-conservative terms, for the hyperbolic part of the system, instead of a treatment in which all terms are treated in a non-conservative way. The non-conservative term concerned is the topographic term in the hydrodynamic momentum equations. The sole diffusive term in the sediment equation has been treated using a primal formulation. Further extensions including (diffusive) turbulent closure terms in the momentum equations are in progress. In addition, a variety of numerical solutions of shallow water flows over a movable bed have been presented and illustrated in an extensive suite of verification and validation tests. The discontinuous Galerkin scheme used showed very good agreement between model simulations versus (semi-)analytical solutions. Moreover, its ability to capture travelling discontinuities without generating spurious oscillations has been demonstrated. The method also allowed the computation of realistic bed profiles, such as the evolution of a trench dredged in a section of the Paraná river, Argentina. For this validation test, our model was able to capture timescales of sediment transport over a dredged river section refilled by an advancing sediment wave front. Our DGFEM method also suitably approximated the flow and sediment transport through a contraction in channel width, a situation present in many natural channels. Finally, a laboratory experiment would be timely in validating both the mathematical and numerical modelling for the latter contraction experiment.

Acknowledgements

It is a pleasure to acknowledge funding from the Institute of Mechanics, Processes and Control Twente (IMPACT) for S.R and P.T., a fellowship of The Royal Netherlands Academy of Arts and Sciences (KNAW) for O.B., a two-year scholarship of the EU Alβan program for P.T., as well as financial assistance from Conicet (Argentina) both for P.T. and C.V.

Appendix A. Algebraic system

A.1. Basis functions and approximations

For each element $K_k \in \mathcal{T}_h$, polynomial approximations of the trial function U and the test functions V are defined as

$$U(t,\mathbf{x})|_{K_k} := \widehat{U}_m(t)\psi_m(\mathbf{x}) \quad \text{and} \quad V(\mathbf{x})|_{K_k} := \widehat{V}_l\psi_l(\mathbf{x}), \quad m, l = 0, \ldots, n_p \tag{A.1}$$

with $(\widehat{\cdot})$ the expansion coefficients, ψ the polynomial basis functions and n_p the number of degrees of freedom. We have split the approximations of the test and trial functions in the space element K into mean and fluctuating parts. The basis functions are defined as

$$\psi_m(\mathbf{x},t) = \begin{cases} 1 & \text{if } m = 0, \\ \phi_m(\mathbf{x}) - c_m & \text{otherwise} \end{cases} \tag{A.2}$$

with

$$c_m = \frac{1}{|K_k|}\int_{K_k} \phi_m(\mathbf{x})\mathrm{d}\mathbf{x} \tag{A.3}$$

and basis functions $\phi_m = 1, \zeta_1, \zeta_2, \zeta_1\zeta_2$ of polynomial order one in terms of the reference coordinates ζ_1, ζ_2 for quadrilateral elements or only the first three functions for triangular elements, and $|K_k| = \int_{K_k} \mathrm{d}K$ is the area of the element K_k.

A.2. Lifting operators

By (3.24) and the fact that $\nabla V_h \subset W_h$, the global lifting operator is defined in [4,5] by

$$\sum_{K_k}\int_{K_k} W_k \mathscr{R}_k \mathrm{d}K = \sum_{S\in\mathscr{S}_I}\int_{\mathscr{S}} \{\!\{TW_k\}\!\}[\![U_4]\!]_k \mathrm{d}\mathscr{S} + \sum_{S\in\mathscr{S}_B}\int_{\mathscr{S}} W_k^{\mathsf{L}} T^{\mathsf{L}}(U_4^{\mathsf{L}} - \widehat{U}_4^{B}) n_k^{\mathsf{L}} \mathrm{d}\mathscr{S}. \tag{A.4}$$

The local lifting operator $\mathscr{R}^{\mathscr{S}}$ is approximated by polynomial approximations as

$$\mathscr{R}^{\mathscr{S}}(\mathbf{x}) = \widehat{R}_j \psi_j(\mathbf{x}) \tag{A.5}$$

with $\widehat{R}_j$ the expansion coefficients of the approximation. By definition, see (3.31), we find that the local lifting operator is only non-zero on the two elements K^{L} and K^{R} directly connected to a face $\mathscr{S}\in\mathscr{S}_I$; hence

$$\int_{K_k^{\mathsf{L}}} W_k \mathscr{R}_k^{\mathscr{S}} \mathrm{d}K + \int_{K_k^{\mathsf{R}}} W_k \mathscr{R}_k^{\mathscr{S}} \mathrm{d}K = \int_{\mathscr{S}} \{\!\{TW_k\}\!\}[\![U_4]\!]_k \mathrm{d}\mathscr{S}. \tag{A.6}$$

Since W is an arbitrary test function, (A.6) is equivalent [4,5] to

$$\int_{K_k^{\mathsf{m}}} W_k \mathscr{R}_k^{\mathscr{S}} \mathrm{d}K = \frac{1}{2}\int_{\mathscr{S}} W_k^{\mathsf{m}} T^{\mathsf{m}} [\![U_4]\!]_k \mathrm{d}\mathscr{S}, \tag{A.7}$$

where $\mathsf{m} = \mathsf{L},\mathsf{R}$ is the index of the left and right elements connected to the face $\mathscr{S}$, respectively. Replacing $\mathscr{R}^{\mathscr{S}}$ by its polynomial expansion, we obtain the following expression:

$$\widehat{R}_{kj}^{\mathsf{m}} \int_{K_k^{\mathsf{m}}} \psi_l \psi_j \mathrm{d}K = \frac{1}{2}\int_{\mathscr{S}} \psi_l^{\mathsf{m}} T^{\mathsf{m}} [\![U_4]\!]_k \mathrm{d}\mathscr{S}. \tag{A.8}$$

The coefficients of the polynomial expansion are

$$\widehat{R}_{kj}^{\mathsf{m}} = \frac{1}{2}(M_{jl}^{-1})^{\mathsf{m}} \int_{\mathscr{S}} \psi_l^{\mathsf{m}} T^{\mathsf{m}} [\![U_4]\!]_k \mathrm{d}\mathscr{S}. \tag{A.9}$$

Similarly, at boundary faces the polynomial expansion of the local lifting operator is

$$\widehat{R}_{kj}^{\mathsf{L}} = (M_{jl}^{-1})^{\mathsf{L}} \int_{\mathscr{S}} \psi_l^{\mathsf{L}} T^{\mathsf{L}} (U_4^{\mathsf{L}} - U_4^{B}) n_k^{\mathsf{L}} \mathrm{d}\mathscr{S}. \tag{A.10}$$

The element mass matrices denoted by $M_{lj} = \int_{K_k} \psi_l \psi_j \mathrm{d}K$ are readily inverted.

A.3. Discretized algebraic system

After discretizing in space, replacing the trial function U and the test function V by their polynomial approximation and inverting the mass matrix in (3.32), we arrive at the following system of ordinary differential equations for the expansion coefficients $\widehat{U}$ of the variables U:

$$M\frac{\mathrm{d}\widehat{U}}{\mathrm{d}t} = \mathscr{L}(\widehat{U}) \tag{A.11}$$

with M akin to the matrix defined in Section A.2 and the operator $\mathscr{L}(\widehat{U})$ defined as

$$\mathscr{L}_{il}(\widehat{U}) = \sum_{K\in\mathscr{T}_h}(-\mathscr{A}_{il} + \mathscr{B}_{il} + \mathscr{E}_{il} - \mathscr{F}_{il}) - \sum_{\mathscr{S}\in S_{I,B}}(\mathscr{C}_{il} + \mathscr{D}_{il} - \mathscr{G}_{il} - \mathscr{H}_{il} + \mathscr{I}_{il}). \tag{A.12}$$

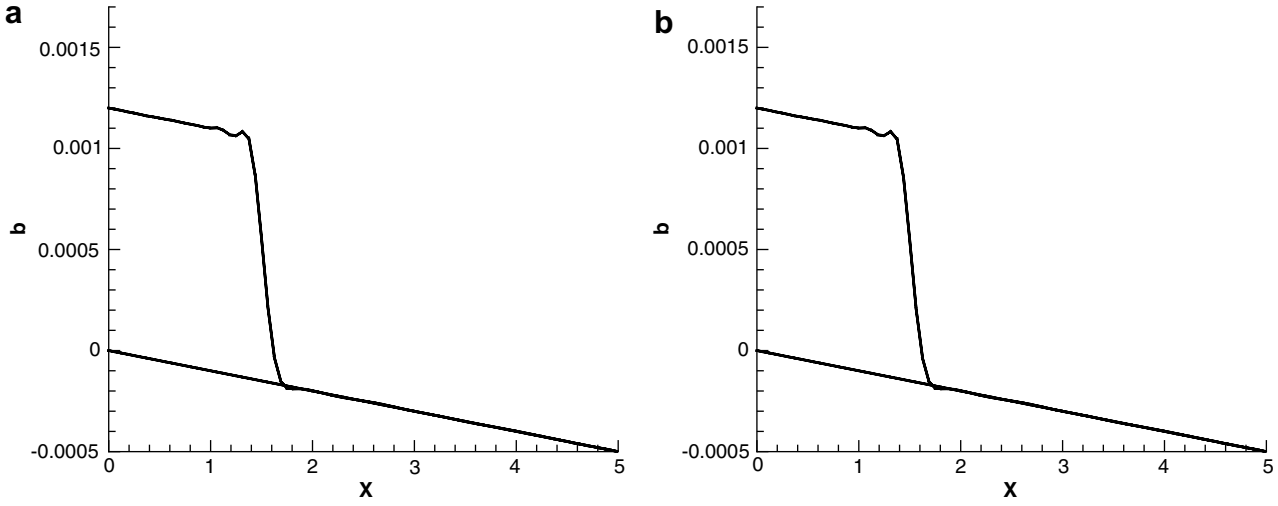

Fig. 16. Profiles of bottom level $b(x,t)$ in a straight channel at time $t = 0.5$ for (a) an effectively first-order time stepping scheme and (b) a third-order time stepping scheme.

Here the terms $\mathscr{A}, \mathscr{B}, \mathscr{C}, \mathscr{D}$, and $\mathscr{E}$ are given by

$$\mathscr{A}_{il} = \int_K \psi_l G_{ikr} U_{r,k} \mathrm{d}K,$$

$$\mathscr{B}_{il} = \int_K \psi_l S_i \mathrm{d}K,$$

$$\mathscr{C}_{il} = \begin{cases} \int_{\mathscr{S}} (\psi_l^{\mathrm{L}} - \psi_l^{\mathrm{R}})(\{\!\{F_{ik}\}\!\} n_k^{\mathrm{L}} + \tilde{H}_i^{\mathrm{nc}}) \mathrm{d}\mathscr{S} & \text{at } \mathscr{S} \in \mathscr{S}_{\mathrm{I}}, \\ \int_{\mathscr{S}} \psi_l^{\mathrm{L}} (F_{ik}^B n_k^{\mathrm{L}} + \widetilde{H}_i^{nc^B}) \mathrm{d}\mathscr{S} & \text{at } \mathscr{S} \in \mathscr{S}_{\mathrm{B}}, \end{cases}$$

$$\mathscr{D}_{il} = \begin{cases} \int_{\mathscr{S}} \{\!\{\psi_l\}\!\} \left(\int_0^1 G_{ikr} (U_r^{\mathrm{R}} - U_r^{\mathrm{L}}) \mathrm{d}\tau n_k^{\mathrm{L}} \right) \mathrm{d}\mathscr{S} & \text{at } \mathscr{S} \in \mathscr{S}_{\mathrm{I}}, \\ \int_{\mathscr{S}} \psi_l^{\mathrm{L}} \left(\int_0^1 G_{ikr} (U_r^B - U_r^{\mathrm{L}}) \mathrm{d}\tau n_k^{\mathrm{L}} \right) \mathrm{d}\mathscr{S} & \text{at } \mathscr{S} \in \mathscr{S}_{\mathrm{B}}, \end{cases}$$

$$\mathscr{E}_{il} = \int_K \psi_{l,k} F_{ik} \mathrm{d}K \tag{A.13}$$

and the terms $\mathscr{F}, \mathscr{G}, \mathscr{H}$, and $\mathscr{I}$ by

$$\mathscr{F}_{il} = \int_K \psi_{l,k} \delta_{i4} T U_{4,k} \, \mathrm{d}K,$$

$$\mathscr{G}_{il} = \begin{cases} \int_{\mathscr{S}} \delta_{i4} \{\!\{T \psi_{l,k}\}\!\} (U_4^{\mathrm{L}} - U_4^{\mathrm{R}}) n_k^{\mathrm{L}} \mathrm{d}\mathscr{S} & \text{at } \mathscr{S} \in \mathscr{S}_{\mathrm{I}}, \\ \int_{\mathscr{S}} \delta_{i4} \psi_{l,k}^{\mathrm{L}} T^{\mathrm{L}} (U_4^{\mathrm{L}} - U_4^B) n_k^{\mathrm{L}} \mathrm{d}\mathscr{S} & \text{at } \mathscr{S} \in \mathscr{S}_{\mathrm{B}}, \end{cases}$$

$$\mathscr{H}_{il} = \begin{cases} \int_{\mathscr{S}} \delta_{i4} [\![\psi_l]\!]_k \{\!\{T U_{4,k}\}\!\} \mathrm{d}\mathscr{S} & \text{at } \mathscr{S} \in \mathscr{S}_{\mathrm{I}}, \\ \int_{\mathscr{S}} \delta_{i4} \psi_l^{\mathrm{L}} T^{\mathrm{L}} U_{4,k}^{\mathrm{L}} n_k^{\mathrm{L}} \mathrm{d}\mathscr{S} & \text{at } \mathscr{S} \in \mathscr{S}_{\mathrm{B}}, \end{cases}$$

$$\mathscr{I}_{il} = \begin{cases} \eta \int_{\mathscr{S}} \delta_{i4} (\psi_l^{\mathrm{L}} - \psi_l^{\mathrm{R}}) \{\!\{\mathscr{R}_k^{\mathscr{S}}\}\!\} n_k^{\mathrm{L}} \mathrm{d}\mathscr{S} & \text{at } \mathscr{S} \in \mathscr{S}_{\mathrm{I}}, \\ \eta \int_{\mathscr{S}} \delta_{i4} \psi_l^{\mathrm{L}} \mathscr{R}_k^{\mathscr{S}} n_k^{\mathrm{L}} \mathrm{d}\mathscr{S} & \text{at } \mathscr{S} \in \mathscr{S}_{\mathrm{B}}. \end{cases} \tag{A.14}$$

A.4. Time stepping scheme

To march in time, in the limit $\epsilon \to 0$, the full system of governing equations (2.7a)–(2.7c) obtains a special coupling in time as in (3.42a), (3.42b) and (3.43). Therefore, we distinguish a slow, sediment time scale t and a fast, hydrodynamic time scale τ, and split (A.11) as follows:

$$M \frac{\mathrm{d}\widehat{U}_h}{\mathrm{d}\tau} = \mathscr{L}_1(\widehat{U}_h(\tau; t), b(t)) \quad \text{and} \quad M \frac{\mathrm{d}\hat{b}}{\mathrm{d}t} = \mathscr{L}_2(\langle \widehat{U}_h \rangle, b), \tag{A.15}$$

where $\widehat{U}_h$ concerns the hydrodynamic part. We aim to march (A.15) to steady-state in τ and solve (A.15) in t. Consequently, a suitable time discretization is the following:

Input: Given initial conditions $\mathbf{u}(\mathbf{x}, 0)$, $h(\mathbf{x}, 0)$ and $b(\mathbf{x}, 0)$
Output: Compute $\mathbf{u}(\mathbf{x}, T_n)$, $h(\mathbf{x}, T_n)$ and $b(\mathbf{x}, T_n)$
Set $n = 0$;
while $t_n < T_n$; $t_n \in [0; T_n]$ **do**
  Set $\hat{U}_h^n$;
  Solve $\hat{U}_h^{(k+1)} = \tilde{\alpha} \hat{U}_h^k + \tilde{\beta} \mathcal{L}_1(\hat{U}_h^k, \hat{b}^n)$ till steady state according to $(*)$;
  Hence $\hat{U}_h^n = \langle \hat{U}_h^n \rangle$;
  Solve $\hat{b}^{(1)} = \hat{b}^n + \Delta t \, \mathcal{L}_2(\langle \hat{U}_h \rangle^n, \hat{b}^n)$ according to $(**)$;
  Solve $\hat{U}_h^{(k+1)} = \tilde{\alpha} \hat{U}_h^k + \tilde{\beta} \mathcal{L}_1(\hat{U}_h^k, \hat{b}^{(1)})$ till steady state according to $(*)$;
  Hence $\hat{U}_h^{(1)} = \langle \hat{U}_h^{(1)} \rangle$;
  Solve $\hat{b}^{(2)} = \frac{3}{4} \hat{b}^n + \frac{1}{4} \hat{b}^{(1)} + \frac{1}{4} \Delta t \, \mathcal{L}_2(\langle \hat{U}_h \rangle^{(1)}, \hat{b}^{(1)})$ according to $(**)$;
  Solve $\hat{U}_h^{(k+1)} = \tilde{\alpha} \hat{U}_h^k + \tilde{\beta} \mathcal{L}_1(\hat{U}_h^k, \hat{b}^{(2)})$ till steady state according to $(*)$;
  Hence $\hat{U}_h^{(2)} = \langle \hat{U}_h^{(2)} \rangle$;
  Solve $\hat{b}^{n+1} = \frac{1}{3} \hat{b}^n + \frac{2}{3} \hat{b}^{(2)} + \frac{2}{3} \Delta t \, \mathcal{L}_2(\langle \hat{U}_h \rangle^{(2)}, \hat{b}^{(2)})$ according to $(**)$;
  $t_n \leftarrow t_n + \Delta t$; $n \leftarrow n + 1$;
end

Algorithm 1. Time stepping algorithm for the morphodynamic model. $(*)$: time stepping algorithm for the flow component (a five-stage explicit Runge–Kutta scheme with appropriate coefficients $\tilde{\alpha}, \tilde{\beta}$, see [16]); $(**)$: stage of a classical three-stage TVD explicit Runge–Kutta scheme [17,1] for the bed component.

Fig. 16 shows results obtained with the proposed first-order time stepping algorithm and the third-order time integration procedure for the graded river test. No visual differences between both time integration procedures were seen.

References

[1] P. Tassi, O. Bokhove, C. Vionnet, Space discontinuous Galerkin method for shallow water flows—kinetic and HLLC flux, and potential vorticity generation, Adv. Water Res. 30 (4) (2007) 988–1015.
[2] S. Rhebergen, O. Bokhove, J.J.W. van der Vegt, Discontinuous Galerkin finite element methods for hyperbolic nonconservative partial differential equations, J. Comput. Phys. 227 (2008) 1887–1922.

[3] D.N. Arnold, F. Brezzi, B. Cockburn, D.L. Marini, Unified analysis of discontinuous Galerkin methods for elliptic problems, SIAM J. Numer. Anal. 39 (5) (2002) 1749–1779.
[4] C. Klaij, Space–time discontinuous Galerkin method for compressible flow. Ph.D. Thesis, University of Twente, 2006. <http://eprints.eemcs.utwente.nl>.
[5] C.M. Klaij, J.J.W. van der Vegt, H. van der Ven, Space–time discontinuous Galerkin method for the compressible Navier–Stokes equations, J. Comput. Phys. 217 (2006) 589–611.
[6] C.B. Vreugdenhil, Numerical Methods for Shallow Water Flow, second ed., Kluwer Academic Publishers, Dordrecht, Netherlands, 1994.
[7] J.A. Cunge, F.M. Holly, A. Verwey, Practical Aspects of Computational River Hydraulics, Pitman, London, 1981.
[8] L.C. van Rijn, Mathematical modeling of morphological processes in case suspended sediment transport. Technical Report 382, Delft Hydraulics Communication, 1987.
[9] W. Wu, W. Rodi, T. Wenka, 3D numerical modeling of flow and sediment transport in open channels, J. Hydraul. Engng. (126) (2000) 4–15.
[10] G. Parker, 1D sediment transport morphodynamics with applications to rivers and turbidity currents, e-book, 2007. <http://cee.uiuc.edu/people/parkerg/>.
[11] F. Engelund, O. Skovgaard, On the origin of meandering and braiding in alluvial streams, J. Fluid Mech. 57 (1973) 289–302.
[12] L.C. van Rijn, Principles of Sediment Transport in Rivers, Estuaries and Coastal Seas. Aqua Publications, 1993, ISBN 90-800356-2-9.
[13] P. Hall, Alternating bar instabilities in unsteady channel flows over erodible beds, J. Fluid Mech. 499 (2004) 49–73.
[14] S. Serra, Flow and bed-load transport over an erodible bed covered with dunes, Master's Thesis, Universidad Nacional del Litoral, FICH, 2007.
[15] W. Ottevanger, Discontinuous finite element modeling of river hydraulics and morphology, with application to the Paraná river, Master's Thesis, Dept. of Applied Mathematics, University of Twente, Enschede, The Netherlands, 2005.
[16] J.J.W. van der Vegt, H. van der Ven, Space–time discontinuous Galerkin finite element method with dynamic grid motion for inviscid compressible flows: I. General formulation, J. Comput. Phys. 182 (2002) 546–585.
[17] C.-W. Shu, TVD time discretizations, SIAM J. Sci. Stat. Comput. 9 (1988) 1073–1084.
[18] O. Bokhove, A.W. Woods, A. Boer de, Magma flow through elastic-walled dikes, Theor. Comput. Fluid Dyn. 19 (2005) 261–286.
[19] E.J. Kubatko, J.J. Westerink, C. Dawson, An unstructured grid morphodynamic model with a discontinuous Galerkin method for bed evolution, Ocean Modell. 15 (2006) 71–89.
[20] P. Tassi, S. Rhebergen, C. Vionnet, O. Bokhove, A discontinuous Galerkin finite element model for morphological evolution under shallow flows, additional appendices, 2007. <http://eprints.eemcs.utwente.nl>.
[21] L. Pesch, A. Bell, W.E.H. Sollie, V.R. Ambati, O. Bokhove, J.J.W. van der Vegt, hpGEM – a software framework for discontinuous Galerkin finite element methods, ACM Trans. Math. Software 33 (4) (2007) 23.